nature communications

Article

https://doi.org/10.1038/s41467-025-63343-z

Circular RNA-based protein replacement therapy mitigates osteoarthritis in male mice

Received: 9 September 2024

Accepted: 18 August 2025

Published online: 26 September 2025

Check for updates

Jinlong Suo[1,13] ✉, Ling Li[2,3,13], Wuyuan Tan[4,5,6,13], Xubin Yin[3], Jinghui Wang[3], Rui Shao[1], Shaokun Sun[3], Si-Kun Guo[3], Jingyi Feng[3], Bao-Qing Gao[7], Ying Wang[3], Meng-Yuan Wei[3], Lijun Wang[8], Heng Feng[3], Xiang Gao[9], Ping Hu[10], Xianyou Zheng[1], Ling-Ling Chen[2,3,11], Guanghua Lei[5,6,12] ✉, Youkui Huang[3] ✉ & Weiguo Zou[1,3,8] ✉

In vitro-transcribed and circularized RNAs (ivcRNAs) represent a robust platform for sustained protein translation, offering promising potential for localized therapeutic delivery in joint diseases. Osteoarthritis (OA), the most prevalent degenerative joint disorder, remains a major clinical challenge due to its progressive nature and the lack of disease-modifying treatments. In this study, we identify *Musashi2 (Msi2)* deficiency in articular chondrocytes as a key contributor to OA pathogenesis. To evaluate the efficacy of ivcRNA-mediated protein replacement therapy, we developed a localized delivery strategy that enables high-yield and prolonged protein expression in chondrocytes. Using a destabilization of the medial meniscus (DMM) mouse model, we demonstrate that intra-articular delivery of ivcRNA encoding MSI2 effectively mitigates OA progression in male mice. Furthermore, therapeutic supplementation of SOX5, a downstream effector of MSI2, via ivcRNA delivery further validates this approach. Our findings establish ivcRNA-based protein replacement as a potential RNA therapeutic strategy for osteoarthritis.

The extraordinary success of mRNA-based vaccines against the coronavirus disease 2019 (COVID-19) pandemic has revitalized interest in RNA therapeutics for clinical applications[1–5]. However, challenges remain regarding mRNA stability, transient expression, immunogenicity[3–5], and potential off-target effects caused by ribosome shifting using chemically modified nucleosides[6]. In contrast, covalently closed circular RNAs (circRNAs) exhibit superior stability, reduced immunogenicity, and enhanced safety compared to both modified mRNAs and viral vector-based therapies[7,8]. Moreover circRNA circumvents the need for costly 5′ capping by using internal ribosomal entry site (IRES) sequences[9–11],

[1]Institute of Microsurgery on Extremities, and Department of Orthopedic Surgery Shanghai Sixth People's Hospital Affiliated to Shanghai Jiao Tong University, School of Medicine, Shanghai 200233, China. [2]School of Life Science and Technology, ShanghaiTech University, Shanghai, China. [3]Key Laboratory of RNA Innovation, Science and Engineering, CAS Center for Excellence in Molecular Cell Science, Shanghai Institute of Biochemistry and Cell Biology, University of Chinese Academy of Sciences, Chinese Academy of Sciences, Shanghai, China. [4]Department of Plastic and Aesthetic Surgery, Xiangya Hospital, Central South University, Changsha, China. [5]Key Laboratory of Aging-related Bone and Joint Diseases Prevention and Treatment, Ministry of Education, Xiangya Hospital, Central South University, Changsha, China. [6]National Clinical Research Center for Geriatric Disorders, Xiangya Hospital, Central South University, Changsha, China. [7]CAS Key Laboratory of Computational Biology, Shanghai Institute of Nutrition and Health, University of Chinese Academy of Sciences, Chinese Academy of Sciences, Shanghai, China. [8]Hainan Institute of Regenerative Orthopedics and Sports Medicine, Hainan Academy of Medical Sciences, Hainan Medical University, Hainan, China. [9]Key Laboratory of Systems Health Science of Zhejiang Province, School of Life Science, Hangzhou Institute for Advanced Study, University of Chinese Academy of Sciences, Hangzhou, China. [10]Guangzhou Laboratory, Guangzhou International Bio Island, Guangzhou, Guangdong, China. [11]New Cornerstone Science Laboratory, Shenzhen, China. [12]Department of Orthopaedics, Xiangya Hospital, Central South University, Changsha, China. [13]These authors contributed equally: Jinlong Suo, Ling Li, Wuyuan Tan. ✉e-mail: suojinlong2015@sibcb.ac.cn; lei_guanghua@csu.edu.cn; huangyoukui@sibcb.ac.cn; zouwg94@sibcb.ac.cn

and obtains low immunogenicity without chemically modified substitutions[10,12]. These advantages position circRNAs as a promising next-generation RNA therapeutic platform[13]. Emerging applications of circRNA-based therapeutics mainly include the use as RNA aptamers[14] and vaccines[15,16]. However, their potential as disease-modifying treatments for osteoarthritis (OA) remains unexplored.

Osteoarthritis (OA) is a chronic degenerative and disabling joint disease characterized by cartilage destruction and osteophyte formation[17–22]. Articular cartilage homeostasis relies on the structural integrity of the extracellular matrix (ECM), particularly the proteoglycan-collagen network[23–25]. Recent study has revealed that $Na_v1.7$ expression in chondrocytes leads to cartilage degeneration and pain[26], suggesting that reversing chondrocyte degeneration alleviates osteoarthritic manifestations. Chondrocytes, the sole resident cells of articular cartilage, maintain ECM equilibrium through a delicate balance of anabolic and catabolic activities[27–29]. Disruptions from aging[30], injury/inflammation[31] and metabolic changes[32] shift this balance, leading to ECM breakdown marked by decreased collagen type II (COL2) and aggrecan alongside elevated matrix metalloproteinase 13 (MMP13) and a disintegrin and metalloproteinase with thrombospondin motifs 5 (ADAMTS5)[33]. Despite these insights, the molecular mechanisms underlying OA remain incompletely understood, and disease-modifying therapies are urgently needed.

RNA-binding proteins (RBPs) critically regulate post-transcriptional processes, including mRNA localization, stability, and translation[34,35]. Some RBPs have been reported to be dysregulated and play a crucial role in inflammation and metabolic changes during OA progression[36]. Recent studies on the role of RBPs in regulating gene functions in OA at different levels have been progressively noticed and reported, including transcription[37], microRNA expression[38], mRNA stability[39], and translational efficiency[40], thus targeting dysregulated RBPs could provide therapeutic strategies for OA treatment. However, whether aging or injury selectively disrupts translation regulating RBPs to exacerbate OA remains unclear. Moreover, safe and effective delivery strategies to restore defective RBP function in OA have not been explored.

Here, we identified Musashi2 (MSI2), a classical RBP, as significantly downregulated in chondrocytes from both OA mice and patients. Functional studies revealed that MSI2 governs chondrocyte metabolism and protects against OA progression. Therapeutically, the local delivery of translatable ivcRNA into the joint cavity targeted articular chondrocytes and exhibited a longer period compared to mRNAs. Osteoarthritis phenotypes of DMM mouse model can be significantly alleviated by intra-articular injection of ivcRNA encoding MSI2 or SOX5.

Results

RNA-binding protein MSI2 is related to osteoarthritis

In order to characterize key RBPs in OA, we systematically investigated an aging-induced OA model, a destabilization of the medial meniscus (DMM) OA model, and human OA cartilage (Fig. 1a). Firstly, we performed RNA-sequencing (RNA-seq) to analyze the differentially expressed RNA-binding proteins involved in the pathogenesis of osteoarthritis (Supplementary Fig. 1a). Our results revealed that 26 RBPs were altered in the DMM mouse model of osteoarthritis (Supplementary Fig. 1a). Additionally, 11 genes were dramatically downregulated during OA development (Supplementary Fig. 1b). Among these RBPs, MSI2 was the foremost candidate due to its significant down-regulation in OA cartilage tissues and its highest base Mean in cartilage tissues (Supplementary Fig. 1b). MSI2 was mainly expressed in the cytoplasm (Supplementary Fig. 1c). Gene ontology (GO) term and pathway analyses of down-regulated genes in mesenchymal stem cells from *Msi2* knockout mice were mainly functionally enriched in extracellular structure organization, extracellular matrix organization, cartilage development, collagen fibril organization, and chondrocyte differentiation, suggesting that MSI2 plays a key role in regulating chondrocyte metabolism and functions (Supplementary Fig. 1d). The significantly reduced expression level of MSI2 was further confirmed in the articular cartilage of DMM mice, suggesting the functional implication of MSI2 in osteoarthritis (Supplementary Fig. 1e, f).

To verify the relationship between MSI2 and osteoarthritis, we then investigated the protein expression profile of MSI2 in aging-induced OA mice. We found that the percentages of MSI2-positive articular chondrocytes were decreased in older mice (7 months old and 2 years old) relative to young mice (4 weeks old), the expression of MSI2 was almost undetectable in the articular cartilage of 2-year-old mice (Supplementary Fig. 1g, h). Importantly, we examined the expression level of MSI2 in human OA cartilage tissue and found significantly reduced MSI2 expression in OA cartilage compared to control tissues (Fig. 1b, c), confirming the clinical relevance of MSI2 in OA.

To further test the potential function of MSI2 on articular cartilage, we found that knockdown of *Msi2* in chondrocytes inhibited its differentiation and led to a decreased expression of Aggrecan, a key indicator of chondrocyte anabolism (Supplementary Fig. 2a, b). We analyzed the transcriptional profile of chondrocytes from *Msi2* knockout mice ($Msi2^{-/-}$). The results showed that *Msi2* deficiency caused abnormal metabolism of articular chondrocytes (Supplementary Fig. 2c). Immunofluorescence staining confirmed the diminished expression of Aggrecan and COL2, which are indicators of anabolism (Supplementary Fig. 2d, e), as well as increased expression of MMP13, an indicator of catabolism (Supplementary Fig. 2d), and increased expression of COL1 in cartilage, an indicator of fibrosis (Supplementary Fig. 2f). GO analysis showed that loss of MSI2 function in chondrocytes is closely related to processes such as cartilage development, chondrocyte differentiation, collagen fibril organization and cell aging (Supplementary Fig. 2g). Thus, these data indicated that MSI2 plays a vital regulatory role in metabolic homeostasis and differentiation of articular chondrocytes. Collectively, these results demonstrated that MSI2 deficiency in chondrocytes may drive the progression of osteoarthritis in mammals.

MSI2 deficiency in chondrocytes contributes to osteoarthritis development

To further explore the function of MSI2 during osteoarthritis progression in vivo, we simulated the progression of osteoarthritis onset in *Msi2* knockout mice through DMM surgery. Histological analysis showed that *Msi2* gene deletion dramatically resulted in articular cartilage erosion or loss, and Osteoarthritis Research Society International (OARSI) score increase, suggesting that MSI2 deficiency exacerbated the progression of osteoarthritis (Supplementary Fig. 3a-b). To further validate the MSI2 function in articular chondrocytes, we constructed a chondrocyte-specific knockout *Msi2* mouse model by crossing *Msi2*-floxed ($Msi2^{fl/fl}$) mice with *Col2-CreERT2* mice (Supplementary Fig. 3c). Next, we induced MSI2 deletion in chondrocyte following tamoxifen administration in adult mice. Histological analysis confirmed that MSI2 was barely expressed in the articular cartilage of $Col2^{CreERT2}$; $Msi2^{f/f}$ (hereafter named *Msi2 CKO*) mice (Supplementary Fig. 3d, e). In addition, immunohistochemical staining of the knee joints in *Msi2 CKO* mice showed the absence of Aggrecan and the increase of ADAMTS5 associated with OA (Supplementary Fig. 3f–i).

After confirming the successful generation of *Msi2 CKO* mice, DMM surgery was performed in 10-week-old mice, and pathological features of the mouse knee joints were examined 2 months later (Fig. 1d). Micro-CT analysis demonstrated that *Msi2 CKO* mice developed accelerated calcification in the meniscus, along with significantly rougher articular surfaces, following DMM treatment when compared to littermate controls (Fig. 1e, f). Consistent with the total loss of MSI2 function, the 18-week-old *Msi2 CKO* mice developed more severe osteoarthritis, as evidenced by with articular cartilage wear and subchondral bone plate thickening, a significantly increased OARSI histopathological score, and a reduction in cartilage thickness as shown

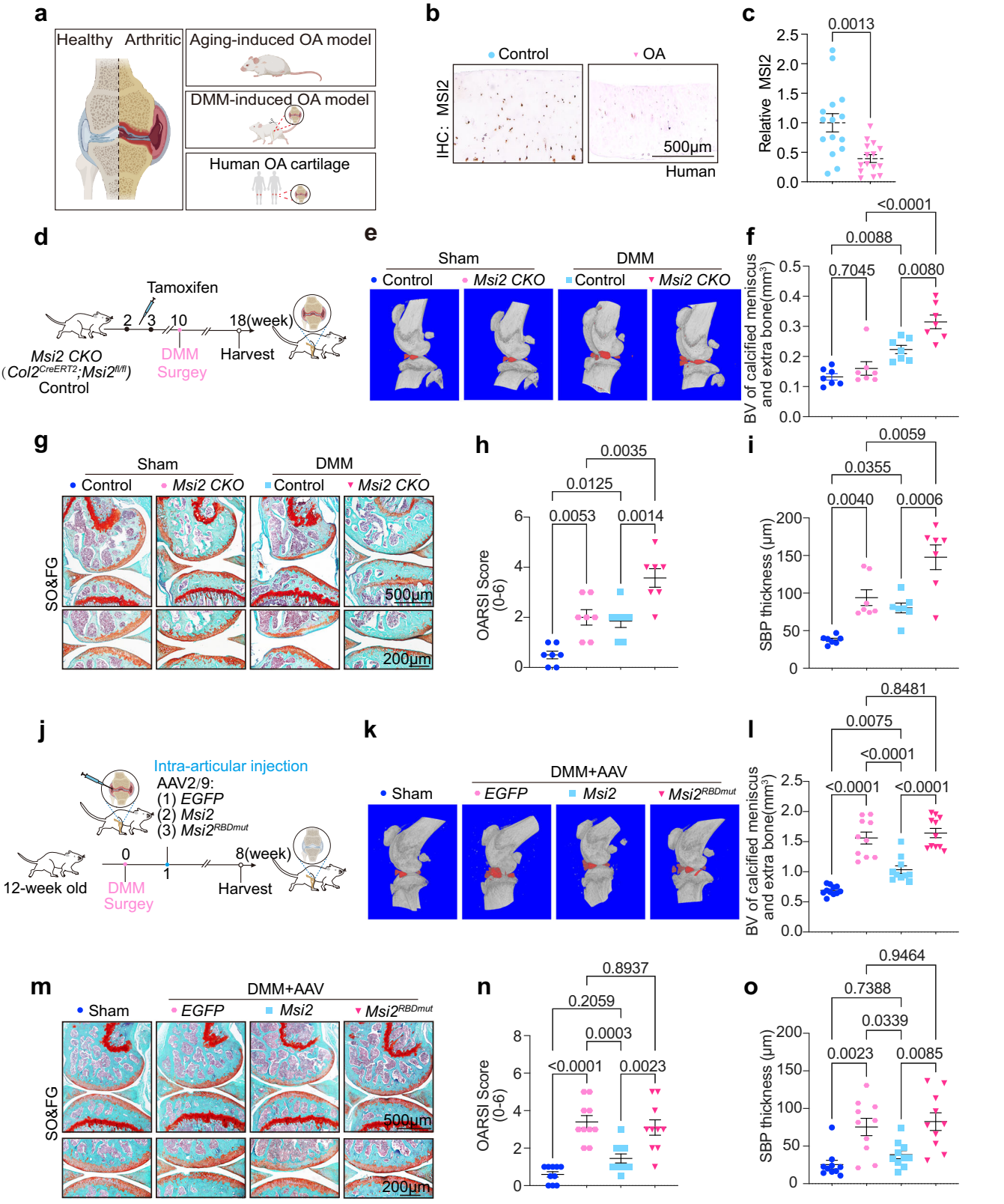

by Safranin O and Fast Green (SO&FG) staining (Fig. 1g–i). Together, these results indicated that loss of MSI2 function in articular chondrocytes promoted osteoarthritic progression in the DMM mouse model.

Based on these observations, we hypothesized that supplementation of deficient MSI2 might alleviate the progression of osteoarthritis in mice. To test this, we performed intra-articular injection of AAV-based gene therapy, which has been demonstrated as an effective strategy for mitigating osteoarthritis[41]. AAV-*Msi2* and AAV-*Msi2*^{RBDmut} were used to overexpress MSI2 and MSI2^{RBDmut} respectively. MSI2^{RBDmut}, a mutant of the RNA-binding domain diminishes the ability of MSI2 to bind to its target RNA[42,43]. We injected AAV-*EGFP*/*Msi2*/*Msi2*^{RBDmut} individually at one week after DMM surgery and then collected the mice's knee cartilage tissue for micro-CT scanning

Fig. 1 | MSI2 is a potential target for osteoarthritis treatment. a Schematic illustration of MSI2 function in three experimental models, including aging-induced osteoarthritis (OA) model, DMM-induced OA model, and human OA cartilage. DMM, destabilization of the medial meniscus. **b** Immunohistochemical staining of MSI2 was performed on paraffin sections of human cartilage from non-weight bearing areas (Control) and weight bearing areas (OA) in patients after arthroplasty. Scale bars = 500 μm. **c** Quantitative analysis of immunohistochemical staining of MSI2 using Image J software (Each group consists of $n = 15$ samples). The data are presented as the Mean with SEM. Statistical significance was determined by two-tailed unpaired t test. **d** Experimental design of tamoxifen (TAM) injection and DMM surgery in *Msi2 CKO* mice and littermate controls. **e** Micro-CT scanning showing calcified meniscus and extra bone in joints from *Msi2 CKO* mice after DMM surgery (calcified meniscus and extra bone are marked in red) ($n = 7$ mice per group). **f** Quantification of the bone volume (BV) of the calcified meniscus and extra bone in (**e**) ($n = 7$ mice per group). The data are presented as the Mean with SEM. Statistical significance was determined by Ordinary one-way ANOVA. **g** Representative images by SO&FG staining of paraffin sections from *Msi2 CKO* mice subjected to the DMM model 8 weeks later ($n = 7$ mice per group). Scale bars=500μm (top), 200μm (bottom). **h** Osteoarthritis Research Society International (OARSI) histopathological score of SO&FG staining in (**g**) ($n = 7$ mice per group). The data are presented as the Mean with SEM. Statistical significance was determined by Ordinary one-way ANOVA. **i** Quantification of subchondral bone plate (SBP) thickness in **(g)** ($n = 7$ mice per group). The data are presented as the Mean with SEM. Statistical significance was determined by Ordinary one-way ANOVA. **j** Schematic of intra-articular injection of AAV expressing MSI2 in DMM-treated mice to evaluate the therapeutic effects against OA. AAV-*EGFP* shown as the negative control, AAV-*Msi2*^{RBDmut} shown as mutation of MSI2 RNA binding domain. **k** Micro-CT scanning showing calcified meniscus and extra bone in joints from DMM-treated mice after intra-articular injection of AAV-*EGFP*, -*MSI2*, -*Msi2*^{RBDmut} (calcified meniscus and extra bone are marked in red) ($n = 11,10,10,11$ mice). **l** Quantification of the BV of the calcified meniscus and extra bone ($n = 11,10,10,11$ mice) in **k**. The data are presented as the Mean with SEM. Statistical significance was determined by Ordinary one-way ANOVA. **m** Representative images of SO&FG staining from DMM-treated mice after intra-articular injection of AAV-*EGFP*, -*MSI2*, -*Msi2*^{RBDmut} ($n = 10$ mice per group). Scale bars=500μm (top), scale bars=200 μm (bottom). **n** OARSI histopathological score of SO&FG staining in (**m**) ($n = 10$ mice per group). The data are presented as the Mean with SEM. Statistical significance was determined by Ordinary one-way ANOVA. **o** Quantification of SBP thickness in (**m**) ($n = 10$ mice per group). The data are presented as the Mean with SEM. Statistical significance was determined by Ordinary one-way ANOVA. Figure 1a, d, j: Created in BioRender. Suo, J. (2025) https://BioRender.com/4byajfm.

and histological analysis 8 weeks later (Fig. 1j). Remarkably, intra-articular delivery of AAV-*Msi2*, compared to AAV-*EGFP* and AAV-*Msi2*^{RBDmut}, predominantly ameliorated OA development induced by DMM surgery, including reduced calcification of the meniscus and extra bone, decreased articular cartilage erosion or loss, attenuated subchondral bone plate thickening, and a decreased OARSI score (Fig. 1k–o). Taken together, these results indicated that MSI2 mitigates OA-induced joint degeneration and progressive loss of articular cartilage, suggesting that MSI2 is a promising therapeutic target for osteoarthritis.

Established local administration of ivcRNA delivery into joint cavity in vivo

AAV-mediated immunotoxicity has constrained the full scale-up of AAV therapy in clinical applications. High dosages of intravenous AAV in clinical settings have resulted in a variety of side effects such as acute kidney injury, thrombocytopenia, and immune-mediated myocardial injury[44]. In vitro synthesized circular RNAs have been shown to exhibit low immunogenicity and high stability, making them suitable for long-term protein expression, and thus representing promising platform for the development of nucleic acid therapy[8,45]. However, it remains unknown whether ivcRNAs can be locally delivered to the articular cavity and act as a replacement protein therapy to effectively target key cell populations in the articular cavity.

To test this feasibility, we synthesized ivcRNA in vitro using a user-friendly permuted-intron–exon (PIE) strategy optimized from *Anabaena* pre-tRNA^{leu} group I intron (Ana_PIE_27nt)[14] (Fig. 2a). Because covalently closed circRNAs lack a 5′cap structure, they depend on internal ribosomal entry site (IRES)-mediated translation[46]. The translation activity of IRESs, which fold into specific structures, require the assistance of cellular auxiliary factors and the eukaryotic initiation factors (eIF), and their ability to initiate translation may exhibit cell type specificity[47,48]. To confirm the most suitable IRES for cartilage-associated cell lines, we adopted four IRESs with high translation efficiency that were screened from our study to synthesize translatable *ivc-IRESs-fLuc* RNAs (Detailed information on the sequences of ivcRNA is provided in Supplementary Data 1, Detailed information on the IRES sequence is provided in Supplementary Data 2). We transfected ivcRNA with these IRESs into chondrocytes and performed a firefly Luciferase (fLuc) luminescence assay to identify the optimal *ivc-IRES-fLuc* for subsequent in vivo administration experiments (Supplementary Fig. 4a). The results showed that *ivc-IRES3-fLuc* achieved the most effective translation in chondrocytes (Supplementary Fig. 4a).

To investigate the translational dynamics of ivcRNA in vivo, we sought to deliver lipid nanoparticles (LNPs)-encapsulated ivcRNA encoding *fLuc* into the articular cavity (Fig. 2b). To evaluate the quality of large-scale-synthesized *ivc-IRES3-fLuc* produced by Ana_PIE_27nt system, the ivcRNA was validated by 4% urea-PAGE gel (Fig. 2c), and ivcRNA purity greater than 80% was quantified by capillary electrophoresis using the PA800 Plus system (Supplementary Fig. 4b). To generate uniformly sized and high-quality ivcRNA-LNPs, we formulated two well-studied ionizable lipid SM-102[49] and EA506[50] with other lipid components to encapsulate *ivc-IRES3-fLuc* respectively using the NanoGenerator Flex microfluidic mixing device (Fig.2b). Of note, the ionizable lipid SM-102 used in the mRNA–LNPs is the clinically approved delivery component in the mRNA-1273 COVID-19 vaccines[51]. Our results revealed that ivcRNA encapsulated with EA506-LNPs diffused throughout the entire body of mice, and the residence in the joint was not evident after 4 h of local intra-articular injection (Supplementary Fig. 4c, d). In contrast, SM-102-LNPs delivering *ivc-IRES3-fLuc* showed relatively specifically at the joints after injection, and the Luciferase activity persisted at high expression level at the joints for two days (Supplementary Fig. 4e, f).

To verify whether the LNPs disseminated after local injection into the joint cavity, we performed intra-articular injection after labelling the ivcRNA-LNPs complex with DiR (1,1′-Dioctadecyl-3,3,3′,3′-Tetramethylindo tricarbocyanine Iodide). Imaging of DiR fluorescence revealed that LNPs consistently remained at the joint site throughout the entire observation period (Supplementary Fig. 4g), which well co-localized with the bioluminescence signal of fLuc (Supplementary Fig. 4h). In summary, we have successfully established a system for producing and locally delivering translatable ivcRNA to the joint cavity.

Locally targeted injection of ivcRNA achieves long-lasting and efficient expression in chondrocytes

To further confirm the long-lasting protein expression of ivcRNA in vivo, we injected PBS, linear *fLuc* mRNA-LNPs, and *ivc-IRES3-fLuc*-LNPs into the joint cavities of mice and observed fLuc expression in the joint cavities daily for 15 days post-injection (Fig. 2d). Physicochemical characterization of ivcRNA-LNPs using dynamic light scattering (DLS) revealed that the particles exhibited an encapsulation efficiency exceeding 90%, an average size ranging from 80 to 100 nm, a polydispersity index below 0.1, and a zeta potential of approximately ±10 mV. These results indicate the successful production of high-quality reporter LNPs (Supplementary Fig. 4i). Next, we performed RT-qPCR assays to systematically evaluate the durability of ivcRNA in

https://doi.org/10.1038/s41467-025-63343-z

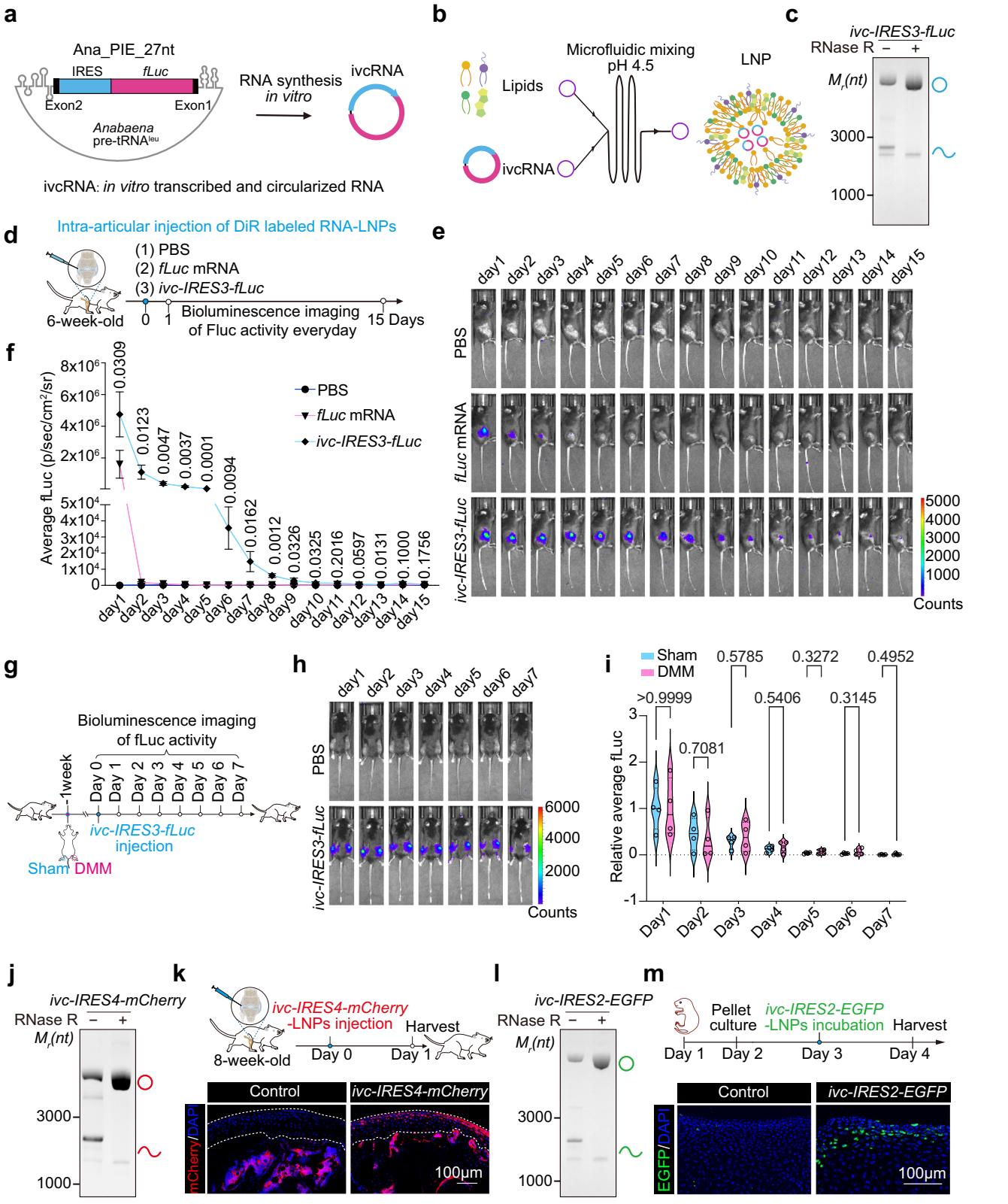

mouse cartilage throughout the experimental timeline. Notably, ivcRNA encoding firefly luciferase exhibited significantly prolonged persistence compared to linear modified mRNAs (Supplementary Fig. 4j). As expected, the luciferase activity in the *ivc-IRES3-fLuc* group was significantly higher than that in the *fLuc* mRNA group, and it was maintained at a high expression level for approximately 7 days, before gradually decreasing around 10 days (Fig. 2e, f). By contrast, the luciferase activity of the *fLuc* mRNA group lasted less than 3 days (Fig. 2e, f). These results demonstrated the advantages of ivcRNA in RNA stability and protein expression.

Interestingly, we also observed that IRES-mediated translation showed no significant difference in the pathological microenvironment

Fig. 2 | Engineered circRNAs encoding fLuc exhibit stable and efficient expression in chondrocytes in vivo. a Schematic diagram of ivcRNA design and synthesis in vitro based on permuted Anabaena group I intron optimized with truncated extraneous sequences (Ana_PIE_27nt system)[14]. ivcRNA, in vitro transcribed and circularized RNA. **b** Schematic diagram of ivcRNA-LNPs (lipid nanoparticles) formulation. The lipid mixture in ethanol and circRNA in aqueous solution were pumped separately into the two inlets of the microfluidic mixing device with a total flow rate of 4 mL/min. **c** Representative image of *ivc-IRES3-fLuc* is analyzed using 4% urea denaturing polyacrylamide gel electrophoresis (Urea-PAGE). Bans of RNA circles are enriched and verified with RNase R. The hollow blue circles indicate circular RNAs, single blue curves indicate nicked RNAs. **d** The pipeline for administering mice to characterize the expression of mRNA/circRNA encoding fLuc in vivo. Intra-articular injection of DiR labeled RNA-LNPs complexes was performed on 6-week-old C57/B6 mice (300 ng RNA per mouse). Bioluminescence imaging of fLuc activity was conducted until the signal returned to background levels. DiR, 1,1′-Dioctadecyl-3,3,3′,3′-Tetramethylindotricarbocyanine Iodide; PBS, phosphate-buffered saline. **e** Represent bioluminescence IVIS images at various time points of the live mice after intra-articular injection of DiR labeled RNA-LNPs complexes. IVIS, in vivo imaging system spectrum. **f** Quantitative statistical analysis of the fluorescence at the injection site for in vivo Luciferase expression at various time points (n = 3 mice per group). The data are presented as the Mean with SD. Statistical significance was determined by multiple two-tailed unpaired t tests in *fLuc* mRNA group and *ivc-IRES3-fLuc* group. **g** Schematic illustration of the experimental pipeline characterizes circRNA injection in sham and DMM-treated mice. Sham (Left leg) and DMM surgery (right leg) were performed in 8-week-old wild-type mice. The dosage of circRNA injection is 500 ng. **h** Bioluminescent images of a representative mice. n = 4 mice per group. Left leg: Sham group; right leg: DMM group. **i** Quantitative statistical analysis of the fluorescence at the injection site (Sham and DMM) for in vivo Luciferase expression (n = 4 mice per group). The data are presented as the violin plot and the number of mice is showed as points in each group. Statistical significance was determined by multiple two-tailed unpaired t test, and p-values are labelled in (**i**). **j** Representative image of *ivc-IRES4-mCherry* RNA is analyzed by 4% urea-PAGE. RNA circles are enriched and verified with RNase R. The hollow red circles indicate RNA circles, single red curves indicate nicked RNA. **k** Immunofluorescence staining of mCherry in articular cartilage of joints from mice after intra-articular injection of *ivc-IRES4-mCherry*-LNPs. n = 3 samples per group. Scale bars = 100 μm. **l** Representative image of *ivc-IRES2-EGFP* is analyzed using denaturing 4% urea-PAGE. RNA circles are enriched and verified with RNase R. The hollow green circles indicate RNA circles; single green curves indicate nicked RNA. **m** Representative microscopy immunofluorescence staining images of a cross section of day-3 cartilage pellet cultures after incubated with *ivc-IRES2-EGFP*-LNPs. n = 3 samples per group. Scale bars = 100 μm. Figure 2 a, b, d, g. k, m: Created in BioRender. Suo, J. (2025) https://BioRender.com/4byajfm.

of OA after DMM surgery, indicating that IRES-driven translation may exhibit resistance to the inflammatory microenvironment caused by DMM (Fig. 2g–i). Collectively, we found that local injection of ivcRNA into the joint cavity of mice enables locally sustained and robust expression longer-lasting than linear mRNA, suggesting ivcRNA is a superior tool for protein replacement therapy in articular cartilage.

Given that MSI2 functions in articular chondrocytes, it is crucial to determine whether SM-102-LNPs can specifically target articular chondrocytes following intra-articular injection. To test this, we screened the well-translated *ivc-IRES4-mCherry* from four IRES-driven ivcRNA constructs (Supplementary Fig. 5a, c), and then injected high-quality *ivc-IRES4-mCherry* into the articular cavity of 8-week-old mice (Fig. 2j–k). Twenty-four hours after ivc-IRES4-mCherry-LNPs delivery, we collected knee cartilage tissue samples for immunofluorescence. The results showed that chondrocytes in the surface layer of articular cartilage were strongly labeled by fluorescent signals (Fig. 2k). In addition, we isolated articular cartilage from neonatal mice, performed pellet culture for 24 h and incubated with the screened and well-translated *ivc-IRES2-eGFP*-LNPs, likewise screened from these four IRESs (Fig. 2l, Supplementary Fig. 5b, c). Consistent with the in vivo results, the superficial zone of cartilage spheres was detected strong green fluorescent signals (Fig. 2m). Together, these data suggest that local intra-articular delivery ivcRNA can effectively target and enable prolonged protein expression in articular chondrocytes.

Engineering circular *Msi2*-based RNA therapy alleviates osteoarthritis

To explore the therapeutic potential of in vitro synthesized translatable ivcRNA, we next attempted to deliver LNP-encapsulated ivcRNA to relieve osteoarthritis. Due to structure-dependent IRES-mediated translation initiation and lack of a structure prediction tool for sequence design to ensure correct IRES folding in the circular conformation[11,52], three types of codon optimization were adopted in combinate with four types of IRESs. Then a group of *ivc-IRES-Msi2* RNAs were synthesized in vitro and transfected into chondrocytes individually for screening the best-translated IRES-mediated coding sequence combinations for subsequent in vivo studies (Fig. 3a, Supplementary Fig. 6a). Through screening we found that codon optimization of *Msi2* was effective to enhance protein expression and obtained the effective combination for *ivc-IRES4-Msi2-optimized-1* (hereafter named *ivc-IRES4-Msi2*) translation in chondrocytes (Fig. 3b, c). A concentration gradient of *ivc-IRES4-Msi2* transfected into chondrocytes progressively promoted chondrocyte differentiation as shown up-regulation of *Acan* and *Col2a1* (Supplementary Fig. 6b, c), validating the roles of MSI2 in chondrocytes using ivcRNA expression. Likewise, the size and uniformity of the LNPs were obtained, as examined by transmission electron microscopy (TEM) and DLS (Supplementary Fig. 6d, e). Importantly, the low immunogenicity of ivcRNA similar to linear modified mRNA as examined that the expression of inflammatory cytokines had no significant induction, suggesting the low toxicity and safety of ivcRNA therapy (Supplementary Fig. 6f, g).

IvcRNA encoding MSI2 also exhibited significantly prolonged persistence compared to linear modified mRNAs in cartilage (Supplementary Fig. 6h). Similar to the result observed in Fig. 2e, protein expression in chondrocytes delivering *ivc-IRES4-Msi2* was significantly higher than that of *Msi2* mRNA delivery (Fig. 3d). The *ivc-IRES4-Msi2* provided long-lasting protein expression till to five days, whereas *Msi2* mRNA delivery was almost metabolically terminated after three days (Fig. 3d). Given the above observation, intra-articular injections of *ivc-IRES4-Msi2*/*Msi2* mRNA/*ivc-IRES3-fLuc* LNPs were performed every week in DMM-treated mice, and the knees of the mice were collected for analysis at 8 weeks after DMM surgery (Fig. 3e). Remarkably, *ivc-IRES4-Msi2* injection significantly alleviated the volume of calcification of the meniscus and extra bone in mice caused by the DMM model, compared to *ivc-IRES3-fLuc* control as shown by micro-CT scans (Fig. 3f, g). However, *Msi2* mRNA injection slightly attenuated the volume of calcification of the meniscus and extra bone (Fig. 3f, g). Given the higher protein expression of ivcRNA than linear mRNA (Fig. 3d), intra-articular injections of *ivc-IRES4-Msi2* more significantly reduced articular cartilage wear, inhibited subchondral bone plate thickening, increased proteoglycan staining, decreased OARSI histopathological score than injections of *ivc-IRES3-fLuc* and *Msi2* mRNA groups (Fig. 3h–j). As expected, ivcRNA-based MSI2 therapy showed significantly increased MSI2 expression compared to injections of *ivc-IRES3-fLuc* and *Msi2* mRNA groups (Fig. 3k, l). Immunohistochemical staining of knee joints confirmed *ivc-IRES4-Msi2* injection alleviated the phenotype of lack of COL2-metabolic markers and excess ADAMTS5-catabolic markers in articular cartilage of mice caused by DMM surgery (Supplementary Fig. 7a–d). Remarkably, the effectively relief effect of osteoarthritis in DMM model was similar to AAV-based gene therapy (Fig. 1j–o and 3e–j), suggesting a promising replacement therapy of ivcRNA.

To further confirm the pathological function depending on a concentration gradient delivering ivcRNA in vivo, injections of 0 ng

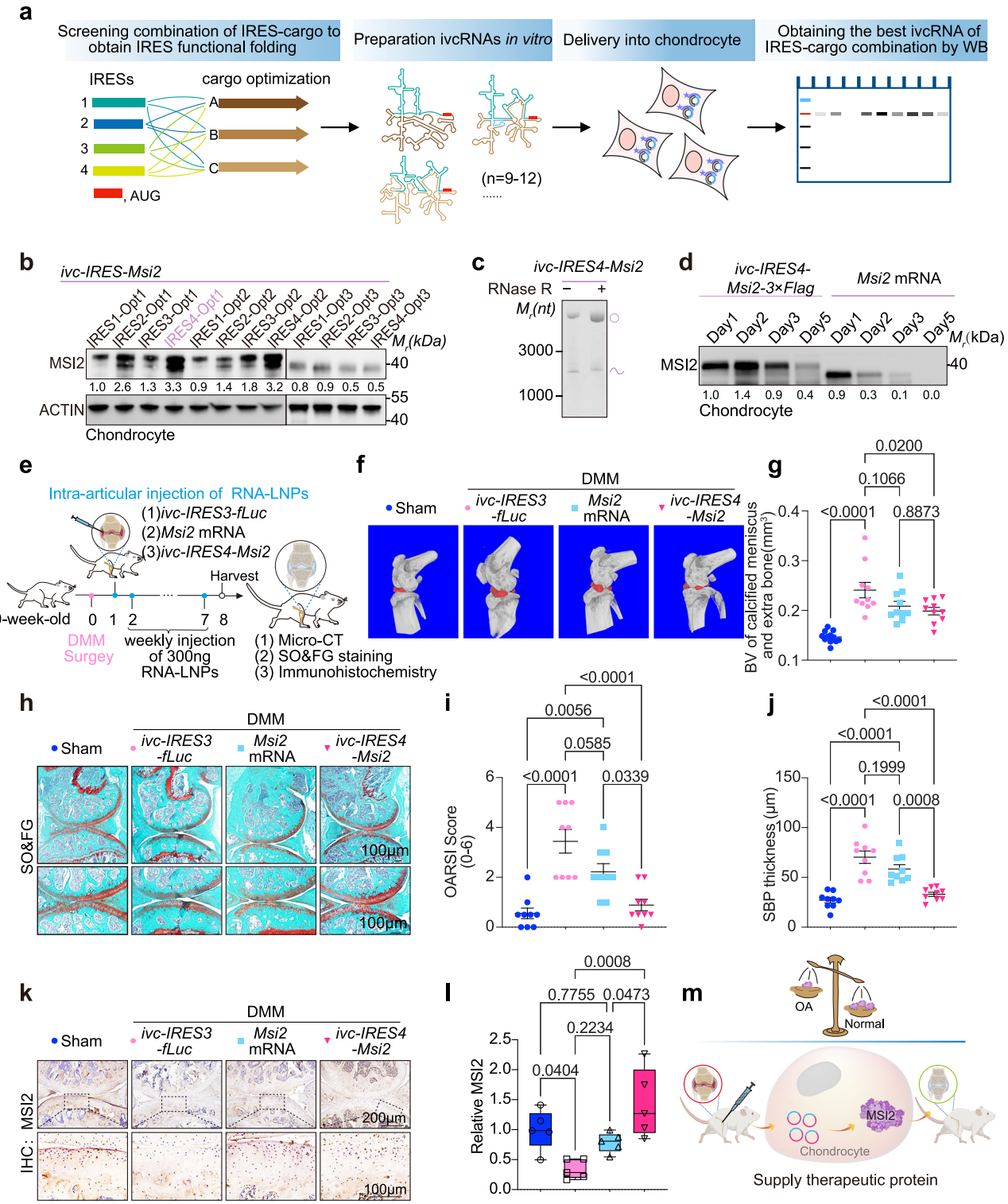

(PBS)/300 ng (Low)/1000 ng (Hig) *ivc-IRES3-fLuc*-LNPs were performed in wild type mice and observed fLuc expression in the joint cavities daily for 7 days after intra-articular injection (Supplementary Fig. 7e). As expected, the examining Luciferase activity in the Hig group was significantly higher compared to the Low group and PBS group (Supplementary Fig. 7f). Injections of 0 ng/100 ng/300 ng *ivc-IRES4-MSi2*-LNPs were performed every week in DMM-treated mice, and the knees of the mice were collected for analysis at 7 weeks after ivcRNA injection (Supplementary Fig. 7g). Concentration gradient delivery of *ivc-IRES4-Msi2* showed gradually alleviated the volume of calcification of the meniscus and extra bone in mice caused by the DMM model, compared to *ivc-IRES3-fLuc* as examined by micro-CT in the DMM model (Supplementary Fig. 7h, i). Taken together, locally intra-articular injection strategy of *ivc-IRES4-Msi2* in a concentration-dependent manner to relieve the progression of osteoarthritis are effective and superior to *Msi2* mRNA therapy (Fig. 3m).

Supplementation of therapeutic SOX5 verifies strategy of ivcRNA-based osteoarthritis treatment

To broaden the strategy of ivcRNA-based replacement therapy, we attempted to apply another target factor contributing to OA. The SOX family has been shown to play an essential role in the maintenance of

Fig. 3 | ivcRNA-based MSI2 therapy alleviates osteoarthritis. a Schematic showing the pipeline of designing and screening engineered ivcRNA encoding MSI2. First, we select different types of IRES elements screened from the viral IRES database, then, optimize the coding sequence (cargo) and combine various IRES elements with the cargo sequence, finally screen combinations of IRES-cargo to obtain IRES functional folding. The prepared in vitro transcribed circRNA deliver into chondrocyte cells to obtain the best ivcRNA of IRES-cargo combination using western blotting (WB). **b** WB analysis of mouse MSI2 expression levels in chondrocytes 24 h after transfection with various *IRES-Msi2* combinations. ACTIN was used as a reference protein. Quantification of MSI2 bands was performed with Image J software. The *IRES-Msi2-Opt1* and *IRES-Msi2-Opt2* plasmids contain a 3 × Flag tag, while the *IRES-Msi2-Opt3* plasmids do not. Opt: Optimized. **c** Representative image of *ivc-IRES4-Msi2* is analyzed using 4% denaturing urea-PAGE. RNA circles are enriched and verified with RNase R treatment. The hollow violet circles indicate RNA circles; single violet curves indicate nicked RNAs. **d** WB analysis of mouse MSI2 expression levels in chondrocytes after transfection with *ivc-IRES4-Msi2-3×Flag* and *Msi2* mRNA. Quantification of MSI2 bands was performed with Image J software. **e** Schematic illustration of intra-articular injection of *ivc-IRES4-Msi2*-LNPs to treatment DMM mice. Two group, Sham and DMM mice, were treated at 10-week-old and monitored to evaluate the therapeutics effects against OA caused by DMM surgery after 8-week-teatment. **f** Micro-CT scans show calcified meniscus and extra bone after intra-articular injection of *ivc-IRES3-fLuc*, *Msi2* mRNA and *ivc-IRES4-Msi2* in DMM model mice (calcified meniscus and extra bone are marked in red) ($n = 12$, 10, 10, 10 mice). **g** Quantification of the BV of the calcified meniscus and extra bone in (**f**) ($n = 12$, 10, 10, 10 mice). The data are presented as the Mean with SEM. Statistical significance was determined by Ordinary one-way ANOVA. **h** Representative images of SO&FG staining of paraffin sections from wild-type mice injected with linear and ivcRNA encoding MSI2 and ivcRNA encoding fLuc after DMM ($n = 9$ mice per group). Scale bars=100μm. **i** OARSI histopathological score for SO&FG staining in (**h**) ($n = 9$ mice per group). The data are presented as the Mean with SEM. Statistical significance was determined by Ordinary one-way ANOVA. **j** Quantification of SBP thickness in (**h**) ($n = 9$ mice per group). The data are presented as the Mean with SEM. Statistical significance was determined by Ordinary one-way ANOVA. **k** Immunohistochemical staining with MSI2 antibody was performed on paraffin sections of knee joints from wild-type mice injected with *ivc-IRES3-fLuc, Msi2* mRNA and *ivc-IRES4-Msi2* after DMM surgery ($n = 5$ samples per group), scale bars = 200 μm (top), scale bars = 100 μm (bottom). **l** Quantification of MSI2 signals in **(k)** by Image J software ($n = 5$ samples per group). The data are presented as the box-and-whisker plots show minimum (Min) to maximum (Max) and all points. Statistical significance was determined by Ordinary one-way ANOVA. Boxes: 25th–75th percentiles; centre line: median; whiskers: 1.5 × IQR. **m** Schematic representation of ivcRNA-based therapy compensates MSI2 to alleviate the phenotypes of OA in DMM mice. The experiments in Fig. 3b, c, d was repeated three times independently and similar results were obtained. The images of knee joint, RNA and mice in Fig. 3a, e, m were adapted from BioRender.com. Created in BioRender. Suo, J. (2025) https://BioRender.com/4byajfm.

chondrocyte homeostasis[53]. Given that MSI2 as a RBP modulating protein translation[42,43], however, the relationship between MSI2 and the SOX family is unclear. We examined the numbers of MSI2 binding elements (MBEs) in the 3′UTR region of *Sox* family members, in detail, the numbers of MBEs in 3′UTR region of SOX11, SOX6 and SOX5 is most abundance (Supplementary Fig. 8a). Additionally, we analyzed the expression profiles of the expression abundance of *Sox* family members in a dataset of single cell sequencing of human articular chondrocytes[54]. Further single-cell sequencing data showed that *Sox5* had the highest expression abundance in human articular chondrocytes (Supplementary Fig. 8b). A recent study has revealed SOX5 as a driver and therapeutic target of rejuvenation, and SOX5 overexpression-based gene therapy can reverse aging-related joint degeneration and progressive loss of articular cartilage[55]. We noted the 3′ untranslated region (3′UTR) of *Sox5* mRNA enriched MSI2 binding sites (G/AU1-3AGU)[43,56](Fig. 4a). To further confirm the *Sox5* mRNA regulated by MSI2, RNA Immunoprecipitation (RIP) assays showed that MSI2 binding to *Sox5* 3′UTR in chondrocytes (Fig. 4b). Additionally, RIP assays demonstrated that MSI2, but not $MSI2^{RBDmut}$, bound to *Sox5* 3′ UTR in stably expressed Flag-MSI2 /Flag-$MSI2^{RBDmut}$ ATDC5 cell line (Supplementary Fig. 9a). Moreover, MSI2 overexpression had no significant effect on the transcriptional level of *Sox5* in ATDC5 cell line (Supplementary Fig. 9b). However. it dramatically promoted the transcriptional level of High Mobility Group Box 2 (HMGB2), which is a target of SOX5[55] (Supplementary Fig. 9c). Importantly, MSI2 overexpression greatly promoted the translation of SOX5 and HMGB2 compared to control and $MSI2^{RBDmut}$ (Fig. 4c, Supplementary Fig. 9d). As expected, the expression level of SOX5 and HMGB2 were notably reduced in *Msi2*-deficient articular cartilage (Supplementary Fig. 9e-h). Particularly the expression level of SOX5 was reduced in the wear region of human OA cartilage (Fig. 4d, e), demonstrating SOX5-HMGB2 axis regulated by MSI2.

To further demonstrate that MSI2 promotes the regulation of SOX5 at the protein translation level rather than at the RNA level. Firstly, we used ActD assay to characterize whether the upregulation of SOX5 by MSI2 is due to mRNA stabilization. After ActD treatment, there was no obvious differences after MSI2 overexpression (Supplementary Fig. 10a). Secondly, we performed reporter assays using GFP expression constructs carrying the 3′UTR sequence of *Sox5* cloned downstream of the GFP coding region. A construct expressing two copies of GFP protein (2×GFP) served as a transfection control. MSI2 overexpression, but not $MSI2^{RBDmut}$, increased the GFP expression of the 3′UTR reporter (Supplementary Fig. 10b, c). Furthermore, overexpression MSI2 or $MSI2^{RBDmut}$ failed to promote GFP expression of the 3′UTR mutant reporter (Supplementary Fig. 10d, e).

Next, we designed and synthesized *ivc-IRES-Sox5* for exploring replacement therapy in OA (Supplementary Fig. 11a). A best-translatable *ivc-IRES3-Sox5-optimized-2* (hereafter named *ivc-IRES3-Sox5*) was selected in chondrocyte (Fig. 4f, g). The ivcRNA-LNPs were formulated as above and the physical properties and immunogenicity of ivcRNA-LNPs were analyzed and verified for subsequent administration in vivo (Supplementary Fig. 11b–d, 6f). ivcRNA encoding SOX5 also exhibited significantly prolonged persistence compared to linear modified mRNAs in cartilage (Supplementary Fig. 11e). Similar to *ivc-IRES4-Msi2*, the *ivc-IRES3-Sox5* also provided long-lasting protein expression till to five days (Fig. 4h).

On the one hand, joint cavity injection of *ivc-IRES3-Sox5* alleviated osteoarthritis after DMM surgery in *CKO* mice (Supplementary Fig. 12a, b), validating the SOX5 functioned in MSI2 downstream. On the other hand, injections of *ivc-IRES3-Sox5*-LNPs/*ivc-IRES3-fLuc*-LNPs were performed every week in DMM-treated mice, and the knees of the mice were collected for analysis after DMM surgery to assess the roles of SOX5 in OA (Fig. 4i). In accordance with *ivc-IRES4-Msi2* based replacement therapy, *ivc-IRES3-Sox5* injection significantly alleviated the volume of calcification of the meniscus and extra bone in mice caused by the DMM model, compared to *ivc-IRES3-fLuc* as examined the volume of calcification of the meniscus and extra bone in mice by micro-CT in the DMM model (Fig. 4j, k). Injections of *ivc-IRES3-Sox5* more significantly reduced articular cartilage erosion or loss, increased proteoglycan staining, and decreased OARSI histopathological score compared to injections of *ivc-IRES3- fLuc* (Fig. 4l-n), as immunohistochemical staining confirmed the significant complementation of SOX5 protein (Fig. 4o, p). Furthermore, SOX5 not only partially promoted Aggrecan expression, which were down-regulated expression in DMM model (Supplementary Fig. 12c, d), but also alleviated the phenotype of excess ADAMTS5-catabolic markers in articular cartilage of mice caused by DMM surgery, as examined by immuno-histochemical staining of knee joints (Supplementary Fig. 12e, f). In general, we established a local injection of ivcRNA-based protein supplementing strategy to effectively alleviate the progression of osteoarthritis (Fig. 4q).

In conclusion, our study identified *Musashi 2* as a promising molecular target for osteoarthritis treatment. By developing an innovative ivcRNA-based delivery platform, we have demonstrated that

https://doi.org/10.1038/s41467-025-63343-z

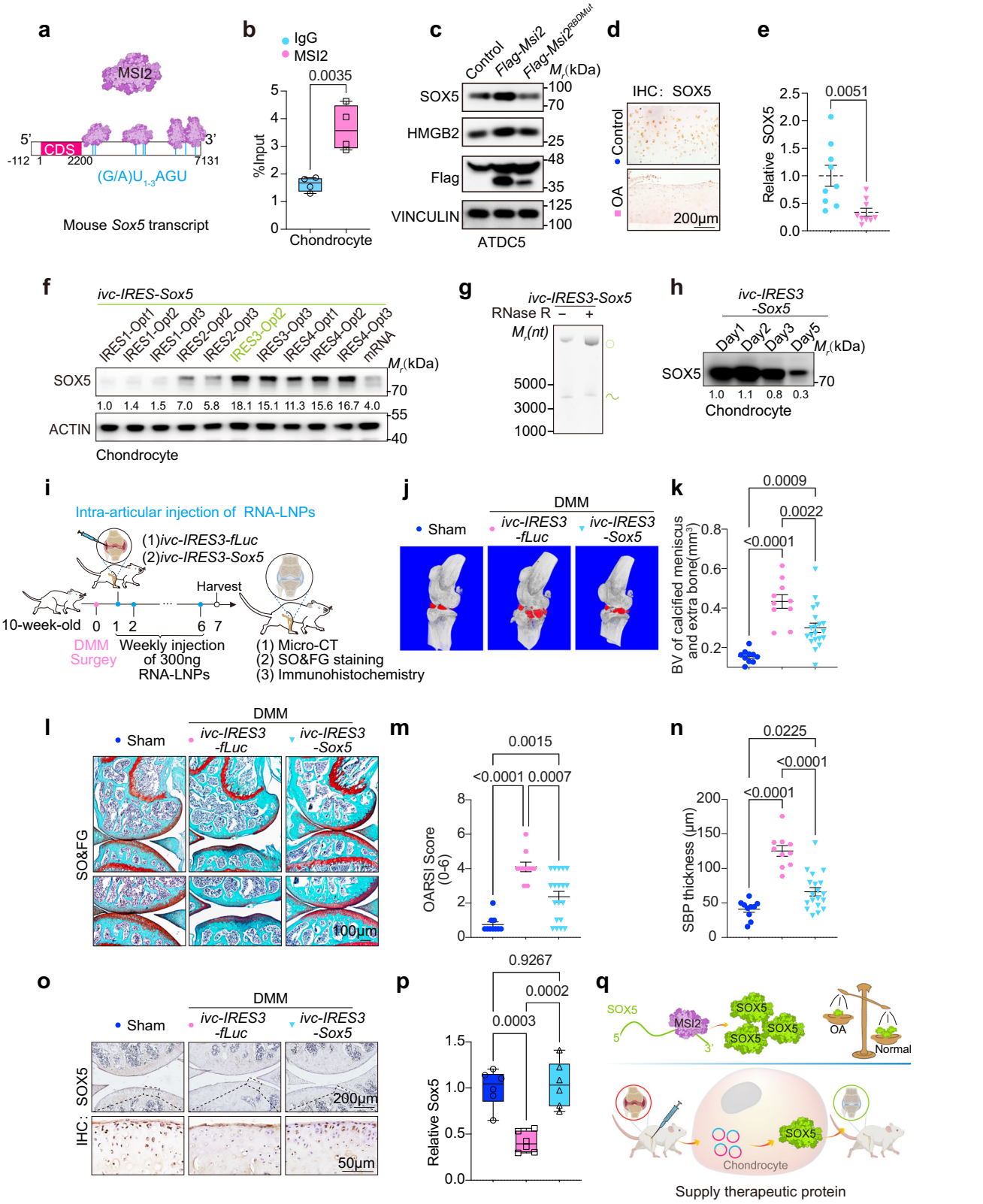

LNP-encapsulated translatable circRNAs can be delivered into the joint cavity and specifically target chondrocytes. This system enables alternative protein expression that effectively alleviates OA progression. As a demonstration, this study highlights the therapeutic potential of ivcRNA-based protein replacement and opens avenues for developing OA treatments.

Discussion

Our study highlights the essential role of MSI2 in osteoarthritis progression and introduces the innovative application of translatable ivcRNA for osteoarthritis therapeutic interventions. In brief, we identified that MSI2, an RNA-binding protein, regulated the *Sox5* mRNA translation contributing to attenuate osteoarthritis progression.

Fig. 4 | ivcRNA-based SOX5 therapy inhibits osteoarthritis progression. **a** Schematic illustration of the mouse *Sox5* transcript (ENSMUST00000038815.13) binding by MSI2 protein. Blue Bars, the putative MSI2 binding elements (MBEs: r(G/A)U_{1-3}AGU). CDS, coding sequence. **b** Coimmunoprecipitated RNAs were analyzed for the enrichment of *Sox5* transcripts with anti-MSI2 antibody or a control rabbit IgG in chondrocytes. The data are presented as the box-and-whisker plots show Min to Max and all points. $n = 4$ biological repeats. Statistical significance was determined by two-tailed unpaired t test. **c** WB analysis of SOX5, HMGB2, VINCULIN and MSI2 protein levels in ATDC5 cells overexpressing *Flag-tagged Msi2* and *Flag-tagged* $Msi2^{RBDmut}$. VINCULIN was used as a reference protein. **d** Immunohistochemical staining with SOX5 antibody was performed on paraffin sections of cartilage from patients with arthroplasty. Scale bars = 200 μm. **e** Quantitative statistics of signals from immunohistochemical staining of SOX5 in (**d**) using Image J software ($n = 9$ samples per group). The data are presented as the Mean with SEM. Statistical significance was determined by two-tailed unpaired t test. **f** WB analysis of mouse SOX5 expression levels in chondrocyte after 24 h of transfection with various *IRES-Sox5* combinations and *Sox5* mRNA. ACTIN was used as a reference protein. Quantification of SOX5 bands was performed with Image J software. **g** Representative image of *ivc-IRES3-Sox5* is analyzed using 4% denaturing urea-PAGE. RNA circles are enriched and verified with RNase R treatment. The hollow green circles indicate RNA circles; single green curves indicate nicked RNAs. **h** WB analysis of mouse SOX5 expression levels in chondrocytes after transfection with *ivc-IRES3-Sox5*. Quantification of SOX5 bands was performed with Image J software. **i** Schematic illustration of intra-articular injection of ivcRNA-LNPs encoding SOX5 to treatment DMM mice. ivcRNA-based therapy treated 10-week-old mice of sham and DMM. Then, the therapeutic phenotypes of OA were evaluated in sham and DMM mice after 7-week-treatment by micro-CT, SO&FG staining and immunohistochemistry. **j** Micro-CT scans show calcified meniscus and extra bone after intra-articular injection of *ivc-IRES3-fLuc*-LNPs, and *ivc-IRES3-Sox5*-LNPs in DMM model mice (calcified meniscus and extra bone are marked in red) ($n = 10, 10, 20$ mice). **k** Quantification of the BV of the calcified meniscus and extra bone in (**j**) ($n = 10, 10, 20$ mice). The data are presented as the Mean with SEM. Statistical significance was determined by Ordinary one-way ANOVA. **l** Representative images of SO&FG staining of paraffin sections from wild-type mice injected with ivcRNA encoding SOX5 and ivcRNA encoding fLuc after DMM surgery ($n = 10, 10, 19$ mice). Scale bars = 100 μm. **m** OARSI histopathological score for SO&FG staining in (**l**) ($n = 10, 10, 19$ mice). The data are presented as the Mean with SEM. Statistical significance was determined by Ordinary one-way ANOVA. **n** Quantification of SBP thickness in (**l**) ($n = 10, 10, 19$ mice). The data are presented as the Mean with SEM. Statistical significance was determined by Ordinary one-way ANOVA. **o** Immunohistochemical staining with SOX5 antibody was performed on paraffin sections of knee joint from wild-type mice injected with ivcRNA encoding SOX5 and ivcRNA encoding fLuc after DMM surgery ($n = 6$ samples per group). Scale bars = 200 μm (top), scale bars = 50 μm (bottom). **p** Quantitative statistics of signals from immunohistochemical staining of SOX5 in **(o)** using Image J software ($n = 6$ samples per group). The data are presented as the box-and-whisker plots show Min to Max and all points. Statistical significance was determined by Ordinary one-way ANOVA. **q** Schematic representation of ivcRNA-based therapy compensates SOX5, a downstream target of MSI2, to alleviate the phenotypes of OA in DMM mice. MSI2 can bind to the 3′UTR of *Sox5* transcripts to promote SOX5 translation, and DMM surgery resulted in a significant decrease in SOX5 protein expression. Injecting ivcRNA-LNPs into the joint cavity of mice after DMM surgery to effectively express SOX5 protein in chondrocytes. Figure 4b, p: Boxes: 25th–75th percentiles; centre line: median; whiskers: 1.5× IQR. The experiments in Fig. 4c, f, g, h was repeated three times independently and similar results were obtained. Figure 4i, q:Created in BioRender. Suo, J. (2025) https://BioRender.com/4byajfm.

Notably, therapeutic potential of targeting MSI2-SOX5 was validated by gene therapy with AAV-*Msi2* and replacement therapy with ivcRNA-*Msi2* and ivcRNA-*Sox5* (Supplementary Fig. 13). Notably, intra-articular delivery of ivcRNA-loaded lipid nanoparticles (LNPs) achieved chondrocyte-specific targeting with low immunogenicity, while exhibiting superior stability, translational efficiency, and prolonged expression compared to linear mRNA.

The identification of disease-relevant RBPs is crucial for understanding OA pathophysiology and developing targeted therapies[36,57]. Through comprehensive screening, we discovered significant downregulation of MSI2 in chondrocytes from both surgically-induced (DMM) OA models and human OA cartilage. This downregulation was particularly pronounced in aging and post-injury contexts (Supplementary Fig. 1e-h). Functional validation using knockout (KO), conditional knockout (CKO), and AAV-based rescue experiments (Fig. 1) established MSI2 as a critical regulator of chondrocyte homeostasis. Mechanistically, MSI2 controls metabolic homeostasis and differentiation of articular chondrocytes, partially through the downstream of SOX5 (Fig. 4). Nevertheless, the molecular mechanism of MSI2 participating in chondrocyte differentiation, metabolism and extracellular matrix organization enriched in GO analysis (Supplementary Fig. 2g), need to investigate further systematically and comprehensively. Not only significant research efforts are ongoing to elucidate the molecular mechanisms focused on gene transcription, but also the regulatory network of RBPs underlying OA remains complex and not yet fully understood.

While μCT can separate trabecular bone from SBP[58], histology provides superior resolution for delineating the tidemark and calcified cartilage layer, which are essential for accurate SBP demarcation. μCT may underestimate SBP thickness due to limited soft-tissue contrast and difficulty in identifying the tidemark. Histology also enables concurrent assessment of osteophyte formation and cartilage degeneration within the same section, ensuring contextual consistency.

The COVID-19 pandemic has accelerated mRNA therapeutic development, yet limitations in stability and translational efficiency persist[3–5]. In our study, synthetic ivcRNA have natural advantages with high stability and low immunogenicity for long-term protein expression, compared to linear mRNA (Fig. 2d-f, Supplementary Fig. 6f). We have successfully delivered translatable ivcRNA to replace the expression of several proteins, including MSI2/SOX5/fLuc/mCherry/EGFP. More importantly, our results suggest that ivcRNA exerts its effects in the joint cavity in a concentration gradient-dependent manner (Supplementary Fig. 7). Through systematic screening of IRES elements and coding sequences (Fig. 3a), we identified highly translatable ivcRNA constructs. However, the mechanisms governing IRES-mediated translation initiation in circRNAs remain incompletely understood, highlighting the need for improved predictive algorithms and design strategies.

As mRNA-based therapies are still in advanced clinical development, their emerging clinical use necessitates thorough safety monitoring for potential post-administration effects[5,59]. By contrast to mRNA vaccines, replacement therapeutic typically require 50-1,000 times higher doses of mRNA[5], which may require repeat dosing with additional toxicological concern[59]. In our study, the locally intra-articular administration, low dosage of ivcRNA-LNPs delivery and effectively targeted articular chondrocytes are achieved lower toxicity risk. We used translatable ivcRNA to compensate for defective protein, MSI2 and SOX5, for osteoarthritis treatments with low dosage of 100 ng or 300 ng ivcRNA for each injection, whereas previous studies showed mRNA therapy for OA with high dosage of 5-50 μg mRNA administration[60]. Additionally, all used in this study of translatable ivcRNA encapsulated in LNPs system also shows low immunogenicity. These advantages of ivcRNA-based therapy greatly eliminate the need for RNA and de-risk potential toxicities of RNA technology. Although this study has showed low-toxicity potential ivcRNA-based replacement therapy, which will still be investigated long-term safety in large animals and clinical phase trials.

For RNA therapeutic applications, realizing delivery system requires to protect RNA against degradation by nuclease and to allow efficient cell-specific or tissue-specific uptake and intracellular release for protein translation[61,62]. Previous studies have shown that LNPs preferentially distribute to the liver when intravenously administered[63], and delivery of LNPs outside the liver is also being pursued preclinically through conjugation of antibodies against cell-

type receptors[63], which indicate that the strategy of administration and choice of LNPs is essential for RNA-based therapy depend on scenarios. We established locally intra-articular injection and tested two reported ionized lipids to achieve LNPs encapsulated ivcRNA locally targeted in the joint cavity (Supplementary Fig. 4c-h). Addressing concerns related to specific cell/tissue targeting and overcoming physical barriers will be essential for expanding the range of targeted diseases. Additionally, our applied SM-102-LNPs system can effectively deliver ivcRNA into articular chondrocytes, which ensures the ivcRNA for effective in OA treatments. However, whether ivcRNA also targeting other cell types in the joint cavity to mitigate OA progression will be determined in the future. In a word, this advancement underscores the exceptional potential of translatable ivcRNA-based replacement therapy with targets, broadening their application in osteoarthritis, holding a potential therapeutic strategy for translatable ivcRNA as an RNA therapy drug to administrate osteoarthritis.

Methods

Mouse lines

Constitutive knockout of *Msi2* (*Msi2*$^{-/-}$) mice were generated as previously described[43], and *Msi2*$^{fl/fl}$ mice were crossed with the type II collagen promoter (*Col2-CreERT2)* strain[64] to generate *Col2-CreERT2*, *Msi2*$^{fl/fl}$ mice. Tamoxifen induction was started at 2 weeks in *Col2 CreERT2*, *Msi2*$^{fl/fl}$ mice, and continued for 5 days with daily injections. This treatment specifically facilitated the excision of exons four and five of the *Msi2* gene in articular chondrocytes. DMM surgery was performed in 8-12-week-old mice.

All mice were maintained on the C57BL/6 background. All mice were housed in a specific pathogen–free environment and treated in strict accordance with protocols approved by the Chinese Academy of Sciences (CAS) Center for Excellence in Molecular Cell Science (CEMCS) (SIBCB-S350-2311-37) or the Committee on the Ethics of Animal Experiments of Central South University. Animals were group-housed (≤5/cage) in ventilated cages with controlled temperature (22 ± 1 °C), humidity (50 ± 10%), and 12-hour light/dark cycles. Provided with nesting materials, PVC tunnels, and wooden chew blocks. Daily health checks by trained staff; weekly cage changes with autoclaved bedding. The experimental mice were euthanized by CO_2 inhalation before tissue collection.

DMM model

Male C57BL/6 mice (10-week-old in Fig.1d, 3e, 4i, and S7g; 12-week-old in Fig. 1j and 8-week-old in Fig. 2g and S3a) underwent surgical destabilization of the medial meniscus (DMM) to induce experimental osteoarthritis. Following anesthesia, the knee joint area was shaved and sterilized. A 3 mm frontal incision was made in the skin overlying the knee joint, exposing the white tendon tissue. The joint capsule, located immediately medial to the patellar tendon, was carefully opened using surgical blades. The patellar tendon was then pivoted laterally and stabilized. Blunt dissection was performed to remove the fat pad covering the intercondylar region, thereby exposing the medial meniscus ligament (MMTL). Any minor bleeding from the fat pad during dissection was meticulously controlled using pressure application. The MMTL was precisely incised using microsurgical scissors to induce destabilization of the medial meniscus. Following this procedure, the joint capsule and skin were sutured. Mice were euthanized and tissue samples were collected for analysis.

AAV injection

Experiments in this study were approved by the Committee on the Ethics of Animal Experiments of Central South University (No: CSU-2022-0457) and carried out in strict accordance with the approved guidelines for the care and use of laboratory animals. 12-week-old, male C57BL/6 mice (mean weight: 27.2 g) were randomly assigned into 4 groups. DMM-AAV2/9-*EGFP* group: AAV2/9-*EGFP* (HanBio, Shanghai, China) was administered to C57BL/6 J mice by intra-articular injection performed post DMM surgery. DMM-AAV2/9-*Msi2* group: 10 μl (1*10^10vg) AAV2/9-*Msi2* (HanBio, Shanghai, China) was administered to C57BL/6 J mice by intra-articular injection performed post DMM surgery. DMM-AAV2/9-*Msi2*^{RBDmut} group: 10 μL (1*10^10vg) AAV2/9-*Msi2*^{RBDmut} (HanBio, Shanghai, China) was administered to C57BL/6 J mice by intra-articular injection performed post DMM surgery. Mice were euthanized at 8 weeks post-AAV injection for histological analyses.

Human research participants (Human Sample)

Human knee articular cartilages were harvested from surgical wastes of patients who underwent total knee replacement with approval by the Committee on the Ethics of Xiangya Hospital, Central South University (No: 2019010305). We received written informed consent. Informed consent has been obtained from patients for the use of human samples. Cartilage form weight-bearing area and non-weight-bearing area were resected to thin slices separately for histological analysis. Cartilages were fixed in 4% paraformaldehyde buffered with phosphate buffered saline (PBS, pH 7.4) for 24 h at 4 °C. Specimens were decalcified with 10% EDTA (pH 7.4) for about 2-4 weeks at 4 °C, embedded in paraffin and 4 μm thick sagittal sections were cut.

In vivo bioluminescent imaging

LNPs encapsulated with mRNA or ivcRNA expressing Luciferase were injected into the knee joint of C57BL/6 J mice. In brief, cutting the skin of the knee joint from the front, mRNA or ivcRNA solution was aspirated into 5 μL microliter syringe (Hamilton, 7634-01). The needle of microliter syringe was slowly inserted into the knee joint. The control group was injected with an equal dose of PBS. After 24 h of intra-articular injection, mice were injected intraperitoneally with 200 μL of 7.5 mg. mL^{-1} D-luciferin (PerkinElmer, 122799). The mice were anesthetized via inhalation of isoflurane 10 min after injection. Bioluminescence imaging was then initiated with a CCD camera (IVIS Spectrum CT, PerkinElmer). Subsequent daily bioluminescence imaging was conducted for 15 days. All bioluminescence data were collected and analyzed with Living Image software (PerkinElmer).

Micro-CT Analysis

Joint tissues were prepared, and Micro-CT analyzed as described previously[64]. Intact knee joints (containing approximately half of the femur and tibia) were isolated from age-matched mice, skin removed and fixed in 70% ethanol. Scans were performed using an instrumented CT system SkyScan1176 (Bruker Biospin). Mouse joints were scanned at a resolution of 9 μm/25 μm for quantitative analysis of redundant bone. Three-dimensional images were reconstructed using fixation thresholding. The volume of redundant bone analyzed in this paper covers the volume of the meniscus. Three-dimensional reconstruction of the knee joint was performed using CTVox software.

For the analysis of calcified meniscus and extra bone, we reconstructed the scanned joint samples (with an accuracy of 9 μm/25 μm) using NRecon software and subsequently calibrated their positions in DataViewer. Following this, we selectively retained the periarticular calcified bone tissues after excluding the femoral, tibial, and patellar components using CTAN software. These regions of interest (ROIs) were then subjected to bone volume (BV) quantification. Representative three-dimensional images were generated using CTvox software, with calcified meniscus and extra bone tissues pseudo colored in red for enhanced visualization.

Histology and immunohistochemistry/immunofluorescence

Knee joints of mice were fixed in 4% paraformaldehyde buffered with phosphate buffered saline (pH 7.4) for 24h-48h at 4 °C. Specimens were decalcified with 10% EDTA (pH 7.4) for 2 weeks at 4 °C, embedded in paraffin and 4 μm/7 μm thick sagittal sections were cut. Sections

were blocked in PBS with 10% horse serum and 0.1% Triton for 1 h and then stained overnight with antibody. Donkey- anti-rabbit Alexa Fluor 488/561 (1:1000; Molecular Probes) was used as secondary antibodies. DAPI (Sigma, D8417) was used for counterstaining. Slides were mounted with anti-fluorescence mounting medium (Dako, S3023), and images were acquired with Olympus FV3000 confocal microscope. DIG labeled in situ hybridization (Roche) and immunohistochemical staining (Dako), and images were acquired with Olympus BX51 microscope.

Safranin O/Fast Green staining

Safranin O/Fast Green staining were performed according to standard protocols. Safranin O/Fast Green staining slides were used to evaluate cartilage degeneration by Osteoarthritis Research Society International (OARSI) scoring system. Each section was assessed by blinded, independent grader and the OARSI histology scoring system (grade 0-6) was used for statistical analysis[65]. The thickness of the subchondral bone plate was measured on Safranin O stained sections. To quantify tibial subchondral bone thickness, we performed systematic measurements at standardized locations along the joint surface, calculating the maximum vertical distance from the calcified cartilage tidemark to the transition zone where subchondral bone meets trabecular architecture. The mean value of these measurements was then calculated to represent the overall subchondral plate thickness, ensuring comprehensive assessment while accounting for potential regional variations in bone morphology. This standardized approach enabled consistent and reproducible evaluation of subchondral bone structural changes across all experimental groups. The measurement protocol was carefully designed to capture true anatomical thickness while avoiding potential confounding factors such as local irregularities or oblique sectioning artifacts.

Alcian Blue staining

Primary chondrocytes were cultured until they reached 80–90% confluence (Passage 2). The cells were then digested and resuspended at a density of 1×10^7 cells/ml. A 12.5 µl droplet of the cell suspension was carefully plated at the center of each well. The plate was incubated at 37 °C for 2 h to allow cell attachment, after which chondrogenic differentiation medium was gently added. The chondrogenic differentiation medium consisted of the following components: DMEM (Dulbecco's Modified Eagle Medium), 10 ng/ml TGFβ3 (Peprotech, Cat#100-36E), 100 nM dexamethasone (Sigma, Cat# D1756), 50 µg/ml L-ascorbic acid 2-phosphate (Sigma, Cat#A8960), 1 mM sodium pyruvate (Sigma, Cat#25-000-CIR), 40 µg/ml proline (Sigma, Cat# P5607), 1% ITS (Insulin-Transferrin-Selenium, Cyagen, Cat# ITSS-10201-10). At designated time points, the micromass cultures were acidified with 0.1 N HCl and subsequently stained with 1% alcian blue (Sigma, Cat# A5268) to assess proteoglycan deposition.

Antibodies

Anti-Flag antibody (F-3165, 1:5000 for WB, Sigma), anti-MSI2 (ab76148, 1:1000 for WB, 1:200 for IHC/IF, Abcam), anti-SOX5 (ab94396, 1:1000 for WB, 1:200 for IHC/IF, Abcam), anti-HMGB2 (ab124670, 1:1000 for WB, 1:200 for IHC/IF, Abcam), anti-MMP13 (18165-1-AP, 1:200 for IHC/IF, Proteintech), anti- Aggrecan (13880-1-AP, 1:200 for IHC/IF, Proteintech), anti-ADAMTS5 (PA5-14350, 1:200 for IHC, Invitrogen), anti-mCherry (AB8181-200, 1:200 for IHC/IF, SICGEN), anti-GFP (66002-1, 1:200 for IHC/IF, Proteintech), anti-VINCULIN (V4505, 1:10000 for WB, Merk), anti-ACTIN (A3854,1:5000 for WB, Sigma).

Plasmid constructions and transfection

To construct shRNA and scramble expression plasmids, DNA sequences of shRNAs and a scramble sequence were individually synthesized and cloned into the pLKO.1-TRC plasmid. To construct *Msi2* and *Msi2*^{RBDmut} overexpression plasmids, DNA sequences for *Msi2* and *Msi2*^{RBDmut} were individually amplified from cDNAs after RT by Phanta Max Super-Fidelity DNA Polymerase (Vazyme Biotech Co., Ltd). Of note, the DNA sequence corresponding to Flag tag was inserted at the 5'-end of DNA sequences for *Msi2* and *Msi2*^{RBDmut} during amplification. All these resulting sequences were amplified and subsequently cloned into the phage vector for protein expression[43]. The 2×GFP plasmid and pEGFP vector were gifts from Prof. Hui Jingyi's group. To clone GFP reporter plasmids, the 3'UTR sequences of *Sox5* were inserted into the polylinker region of the pEGFP vector. Point mutations were introduced by a 2-step PCR method. And plasmids were extracted using the SPARKeasy Superpure Midi Plasmid Kit (Shandong Sparkjade Biotechnology Co., Ltd.).

To construct ivcRNA template plasmid, the DNA sequences of origin *Msi2* / *EGFP* / *mCherry* / *fLuc* was amplified from cDNA. All related IRES element sequences and the optimized *Msi2* and *Sox5* sequences were synthesized in Genscript Biotech Corporation. Template plasmid for ivcRNA containing PIE elements, IRES and coding regions were cloned into linearized pUC57 plasmid vector. Sequences for ivcRNA were listed in Supplementary Data 1.

Isolation of mouse chondrocyte and Pellet culture

For chondrocyte isolation, articular cartilage is dissected from the femoral heads, femoral condyles, and tibial plateaus of hind legs from neonatal mice (P1–P7). Typically, both hind legs from one mouse yield ~50,000–200,000 primary chondrocytes after collagenase II digestion (0.2–0.4%, two-step digestion: Initial digestion in complete digestion buffer for 2 h at 37 °C in a humidified incubator. Secondary digestion in half-strength digestion buffer for 6-8 h. Detailed components as previously described[64]). Following digestion, the cell suspension was filtered through a 70 μm cell strainer and cultured in complete α-MEM medium [supplemented with 10% fetal bovine serum and 1% penicillin/streptomycin (Gibco)] for 3-4 days. To minimize passaging and ensure sufficient cell numbers, cartilage from 4–6 mice (8–12 legs) is pooled, generating-0.5–1.2 million cells at passage 0 (P0). Experiments are performed with P0 or P1 cells to retain chondrogenic capacity. Primary chondrocytes were utilized for RNA sequencing analysis to obtain baseline gene expression profiles, while first-passage (P1) chondrocytes were employed for micromass culture experiments to assess differentiation potential.

For pellet culture: The chondrocyte pellets were generated by centrifuging 2 ~ 4×10^5 cells at 800 × g for 5 min in 15 mL conical tubes, then maintained in chondrogenic medium consisting of α-MEM medium supplemented with 1% ITS, 50 µg/mL ascorbate, 40 µg/mL proline, 0.1 µM dexamethasone, and 10 ng/mL TGF-β3. The pellets were cultured for 7 days with medium changes every 2-3 days before processing for histological analysis. This standardized protocol ensures consistent 3D culture conditions that promote extracellular matrix production while maintaining chondrocyte phenotype.

Translatable ivcRNA design

An optimized Permuted Intron-Exon (PIE) splicing system from *Anabaena* pre-tRNA was chosen for in vitro mRNA circularization, offering an efficient circularization method for long circRNA construction without enzymatic treatment[14] This system includes permuted split fragments of group I catalytic introns corresponding to *Anabaena* pre-tRNA with homology arms at both ends and IRES element upstream of the open reading frame.

Various types of internal ribosome entry site (IRES) elements from viral IRES database were selected to initiate ivcRNA translation. All related IRES element and cargo sequences are listed in Supplementary Data 1, 2.

To improve the translation efficiency of translatable ivcRNA, codon optimization was performed on the protein open reading sequence using various optimization tools, OptimWiz (https://climsprod.genewiz.com.cn /Toolbox/CodonOptimization), Jcat (http://www.jcat.de)

and, ThermoFish (https://www.thermofisher.cn/order/geneartgenes/projectmgmt). The optimized gene sequences were synthesized in Genscript. Template plasmid for ivcRNA containing PIE elements, IRES and coding regions were cloned into linearized pUC57 plasmid vector.

In vitro synthesis and purification of translatable ivcRNA

Templates plasmids were linearized with XbaI (NEB, R0145L) and purified. RNAs were transcribed in vitro using RiboMAX^{TM} Large Scale RNA Production System-T7 (Promega, P1300). Each 20 μL IVT reaction system contained 500 ng of template and was incubated at 37 °C for 3 h. After transcription reaction, IVT templates were subsequently degraded with 2 μL DNaseI for 30 min at 37 °C. For ivcRNA enrichment and purification, the 20-μL reaction products were then poly(A) tailed in a 50 μL reaction system using *E.coli* Poly(A) Polymerase (Tinzyme, GMP-M012) with 5 mM ATP and 15U poly(A) polymerase at 37 °C for 2 h. Following this, the poly(A) tailed RNA samples were treated with 5U of RNase R per 100 μL reaction at 37 °C for 90 min. The remaining RNA was column purified using Hipure RNA pure Micro Kit (Magen, R2144-03), quantified with a Nanodrop One spectrophotometer and verified for purity via 4% denaturing urea-PAGE analysis containing 8 M urea dissolved in Tris-Borate-EDTA (TBE) running buffer. The integrity and size distribution of ivcRNA were analyzed using capillary electrophoresis on the SCIEX PA800 Plus system.

mRNA synthesis

The mRNA was synthesized in Genscript Biotech Corporation. The used *fLuc* mRNA (SC2346, Genscript) was synthesized with Cap1 structure, 100 poly (A) tail and m1Ψ modified whole sequence. For *Msi2* and *Sox5* mRNA, gene coding sequences were firstly optimized in mouse host with OptimumGene tool by Genscript, then were cloned into in vitro transcription (IVT)-mRNA production template plasmid carrying a T7 promoter, Kozak sequence, 5′ and 3′UTR and 100 poly(A) tail. IVT-mRNA was produced with modified m1Ψ-nucleoside, Cap1 structure and 100 poly(A) tail and was dissolved in RNase-Free distilled water.

Lipid nanoparticle Formulation

Each lipid component, including EA506, SM-102 (MCE), 1,2-dioleoyl-sn-glycero-3-phosphoethanolamine (DOPE), 1,2-distearoyl-sn-glycero-3-phosphocholine (DSPC), cholesterol, 1,2-dimyristoyl-rac-glycero-3-methoxypolyethylene glycol-2000 (DMG-PEG2000) was dissolved in ethanol (Sigma). For SM-102-LNPs, ethanolic lipid phase mixture was prepared with molar ratios of SM-102: DSPC: cholesterol: DMG-PEG2000 at 50:10:38.5:1.5; For EA506-LNPs, ethanolic lipid phase mixture was prepared with molar ratios of EA506: DSPC: cholesterol: DMG-PEG2000 at 38:30:30:2. The ivcRNA in aqueous phase was prepared in 25 mM acetate buffer (pH 4.5). The ivcRNA then packaged into lipid nanoparticles was performed using NanoGenerator Flex-M microfluidic mixing system (PreciGenome, California, USA) according to manufacturer's instructions. Briefly, the Lipid and RNA phases were mixed at a 1:3 volume ratio (For SM-102-LNPs, molar ratio N/P = 6:1; For EA506-LNPs, molar ratio N/P = 15:1, ionizable lipid to RNA) and at a flow rate of 4 mL/min. After mixing, formulations were dialyzed against 1 × PBS at 4 °C overnight in Slide-A-Lyzer cassettes with a molecular weight cutoff of 10 kD (Thermo Fisher Scientific, 66380) to remove the ethanol and restore the pH to neutral. They were then concentrated to desired levels using Amicon Ultra filters with a molecular weight cutoff of 100 kD (Milipore, UFC810024).

For ivcRNA delivery into cell line in vitro, selective organ targeting (SORT)-LNPs were used as previous reported with slight modifications[66]. Briefly, ethanolic lipid phase mixture was prepared with molar ratios of 5A2-SC8: DOPE: cholesterol: DMG-PEG2000 at 15:15:30:3. 5A2-SC8 was synthesized by our cooperation Lab (Fajun Nan, State Key Laboratory of Drug Research, Shanghai Institute of Materia Medica, Chinese Academy of Sciences). ivcRNA was diluted in DPBS as aqueous phase (aq.). These two solutions of phase were rapidly mixed at an aqueous to ethanol ratio of 1/1 by volume (1/1, aq./ethanol, vol./vol.) to satisfy a final weight ratio of 36.88/1 (total lipids/RNA), then incubated for 15 min at room temperature for cell transfection.

Lipid Nanoparticle Characterization

Particle size and polydispersity (PDI) were measured using dynamic light scattering (Zetasizer Pro, Malvern Panalytical) in PBS. Zeta potential was measured using the same instrument in double-distilled water. Size data is reported as the largest intensity mean peak average, which constituted >95% of the nanoparticles present in the sample. The encapsulation efficiency of ivcRNA or mRNA was determined by Quanti-iT RiboGreen RNA assay (Thermo Fischer Scientific) according to manufacturer's instructions.

Transmission Electron Microscopy (TEM) analysis of ivcRNA-LNPs

To prepare LNPs for TEM imaging, LNPs were diluted in 1 × PBS solution and negative staining was performed with 2% uranyl acetate. LNPs was placed on a carbon-coated copper grid, dried and analyzed using a FEI Tecnai G2 Spirit Twin transmission electron microscope.

The transfection of ivcRNA in vitro

A549 cell line (SCSP-503) was provided by the Cell Bank, Chinese Academy of Science (CAS), and was cultured in F-12K supplemented with 10% fetal bovine serum and 1% GlutaMax. For A549 cells transfected prior to immunogenicity characterization, 200 ng of RNA and poly(I:C) were reverse transfected into 3×10^5 cells/1 mL per well of a 12-well plate using selective organ targeting (SORT) method detailed in **Lipid nanoparticle Formulation**. For ATDC5, C3H10 and chondrocyte progenitor cells, 200 ng of RNA was transfected into 3×10^5 cells/1 mL per well of a 12-well plate to assess protein expression level using SORT transfection system.

RNA isolation, qRT-PCR

Cells were washed with DPBS and total RNAs were exacted after 24 h transfection with TRIzol (Invitrogen) according to the manufacturer's protocol. Synthesis of first-strand cDNA from total RNA was performed with SuperScript III (Invitrogen) according to the manufacturer's instructions. The quantitative (q)PCR reaction was carried out by using SYBR Green Realtime PCR Master Mix (TOYOBO) and a StepOnePlus real-time PCR system (Applied Biosystems). Threshold cycle values (Ct) were processed according to the comparative Ct method. Gene expression levels were normalized to the expression of housekeeping gene *Hprt* or 18S and presented relative to mock transfection controls. qPCR primer sequences were listed in Supplementary Data 3.

RNA seq and Single cell RNA seq analysis

We extracted articular chondrocytes from Msi2 knockout mice and littermate control mice and obtained RNA for transcriptome sequencing (fold change greater than 1 and P value less than 0.05). The data were analyzed on the free online platform of Majorbio Cloud Platform (www.majorbio.com). We extracted articular chondrocytes from DMM mice and Sham control mice and obtained RNA for transcriptome sequencing (fold change greater than 1.2 and P value less than 0.05). The processed sequencing data is stored in the NCBI Sequence Read Archive (SRA) database with accession number SRR34918750-SSR34918757 (BioProject: PRJNA1303435). Human single-cell sequencing data were obtained from the database uploaded by Sun et al. [54]. We re-clustered the single-cell sequencing of articular cartilage from healthy men, and the clustering metrics were referred to Ji[67] and Sun[54] et al.

Display items. The images of human, mice, knee joint and other icons in Fig 1a, d, j, 2a, b, d, g, k, m, 3a, e, m, 4a, i, q, S3a, S4c, e, S7e, g, S13

were adapted from BioRender.com, and these images have been adapted by the author for use in the manuscript. Liscence: Created in BioRender. Suo, J. (2025) https://BioRender.com/4byajfm.

Statistical analysis

All quantitative data were presented as the mean ± SD or mean ± SEM and analyzed using GraphPad Prism 9 software by unpaired *t* test (two-sided), one-way ANOVA and two-way ANOVA analysis.

Reporting summary

Further information on research design is available in the Nature Portfolio Reporting Summary linked to this article.

Data availability

All data needed to evaluate the conclusions in the paper are present in the paper and/or the Supplementary Materials. Transcriptomic data analyzed in this study are available in the SRA database (BioProject Number: PRJNA 1303435, Detail SRA Number: SRR34918750-SSR34918757), The data link as follows: https://www.ncbi.nlm.nih.gov/sra?term=SRP607550. Source data are provided with this paper. ivcRNAs sequences have been deposited in Supplementary Data 1. IRES sequences have been deposited in Supplementary Data 2. Source data are provided with this paper.

References

1. Baden, L. R. et al. Efficacy and Safety of the mRNA-1273 SARS-CoV-2 Vaccine. *N. Engl. J. Med* **384**, 403–416 (2021).
2. Walsh, E. E. et al. Safety and immunogenicity of two RNA-based Covid-19 vaccine candidates. *N. Engl. J. Med* **383**, 2439–2450 (2020).
3. Parhiz, H., Atochina-Vasserman, E. N. & Weissman, D. mRNA-based therapeutics: looking beyond COVID-19 vaccines. *Lancet* **403**, 1192–1204 (2024).
4. Qin, S. et al. mRNA-based therapeutics: powerful and versatile tools to combat diseases. *Signal Transduct. Target Ther.* **7**, 166 (2022).
5. Rohner, E., Yang, R., Foo, K. S., Goedel, A. & Chien, K. R. Unlocking the promise of mRNA therapeutics. *Nat. Biotechnol.* **40**, 1586–1600 (2022).
6. Mulroney, T. E. et al. N(1)-methylpseudouridylation of mRNA causes +1 ribosomal frameshifting. *Nature* **625**, 189–194 (2024).
7. Pardi, N., Hogan, M. J., Porter, F. W. & Weissman, D. mRNA vaccines - a new era in vaccinology. *Nat. Rev. Drug Discov.* **17**, 261–279 (2018).
8. Liu, C. X. & Chen, L. L. Circular RNAs: characterization, cellular roles, and applications. *Cell* **185**, 2016–2034 (2022).
9. Wesselhoeft, R. A., Kowalski, P. S. & Anderson, D. G. Engineering circular RNA for potent and stable translation in eukaryotic cells. *Nat. Commun.* **9**, 2629 (2018).
10. Wesselhoeft, R. A. et al. RNA Circularization Diminishes Immunogenicity and Can Extend Translation Duration In Vivo. *Mol. cell* **74**, 508–520 e504 (2019).
11. Chen, R. et al. Engineering circular RNA for enhanced protein production. *Nat. Biotechnol.* **41**, 262–272 (2023).
12. Liu, C. X. et al. RNA circles with minimized immunogenicity as potent PKR inhibitors. *Mol. cell* **82**, 420–434 e426 (2022).
13. Dolgin, E. Why rings of RNA could be the next blockbuster drug. *Nature* **622**, 22–24 (2023).
14. Guo, S. K. et al. Therapeutic application of circular RNA aptamers in a mouse model of psoriasis. *Nat. Biotechnol.* (2024).
15. Li, H. et al. Circular RNA cancer vaccines drive immunity in hard-to-treat malignancies. *Theranostics* **12**, 6422–6436 (2022).
16. Qu, L. et al. Circular RNA vaccines against SARS-CoV-2 and emerging variants. *Cell* **185**, 1728–1744 e1716 (2022).
17. Hamerman, D. The biology of osteoarthritis. *N. Engl. J. Med.* **320**, 1322–1330 (1989).
18. Katz, J. N., Arant, K. R. & Loeser, R. F. Diagnosis and Treatment of Hip and Knee Osteoarthritis: A Review. *JAMA* **325**, 568–578 (2021).
19. Hunter, D. J. & Bierma-Zeinstra, S. O. steoarthritis *Lancet* **393**, 1745–1759 (2019).
20. Loeser, R. F. et al. Microarray analysis reveals age-related differences in gene expression during the development of osteoarthritis in mice. *Arthritis Rheum.* **64**, 705–717 (2012).
21. Sinusas, K. Osteoarthritis: diagnosis and treatment. *Am. Fam. Physician* **85**, 49–56 (2012).
22. Martel-Pelletier, J. et al. Osteoarthritis. *Nat. Rev. Dis. Prim.* **2**, 16072 (2016).
23. Nordberg, R. C. et al. Recent advancements in cartilage tissue engineering innovation and translation. *Nat. Rev. Rheumatol.* **20**, 323–346 (2024).
24. Rahmati, M., Nalesso, G., Mobasheri, A. & Mozafari, M. Aging and osteoarthritis: Central role of the extracellular matrix. *Ageing Res Rev.* **40**, 20–30 (2017).
25. Rapp, A. E. & Zaucke, F. Cartilage extracellular matrix-derived matrikines in osteoarthritis. *Am. J. Physiol. Cell Physiol.* **324**, C377–c394 (2023).
26. Fu, W. et al. Na(v)1.7 as a chondrocyte regulator and therapeutic target for osteoarthritis. *Nature* **625**, 557–565 (2024).
27. Zheng, L., Zhang, Z., Sheng, P. & Mobasheri, A. The role of metabolism in chondrocyte dysfunction and the progression of osteoarthritis. *Ageing Res Rev.* **66**, 101249 (2021).
28. Akkiraju, H. & Nohe, A. Role of chondrocytes in cartilage formation, progression of osteoarthritis and cartilage. *Regeneration. J. Dev. Biol.* **3**, 177–192 (2015).
29. Wu, X. et al. Kindlin-2 preserves integrity of the articular cartilage to protect against osteoarthritis. *Nat. Aging* **2**, 332–347 (2022).
30. Baker, D. J. et al. Clearance of p16Ink4a-positive senescent cells delays ageing-associated disorders. *Nature* **479**, 232–236 (2011).
31. Lieberthal, J., Sambamurthy, N. & Scanzello, C. R. Inflammation in joint injury and post-traumatic osteoarthritis. *Osteoarthr. Cartil.* **23**, 1825–1834 (2015).
32. Liu, Q. et al. DDX5 inhibits hyaline cartilage fibrosis and degradation in osteoarthritis via alternative splicing and G-quadruplex unwinding. *Nat. Aging* **4**, 664–680 (2024).
33. Consortium, A. B. et al. A framework of biomarkers for skeletal aging: a consensus statement by the Aging Biomarker Consortium. *Life Med.* **2** (2023).
34. Corley, M., Burns, M. C. & Yeo, G. W. How RNA-binding proteins interact with RNA: molecules and mechanisms. *Mol. Cell* **78**, 9–29 (2020).
35. Hentze, M. W., Castello, A., Schwarzl, T. & Preiss, T. A brave new world of RNA-binding proteins. *Nat. Rev. Mol. Cell Biol.* **19**, 327–341 (2018).
36. Xiang, M., Liu, L., Wu, T., Wei, B. & Liu, H. RNA-binding proteins in degenerative joint diseases: A systematic review. *Ageing Res. Rev.* **86**, 101870 (2023).
37. Yoon, D. S. et al. TLR4 downregulation by the RNA-binding protein PUM1 alleviates cellular aging and osteoarthritis. *Cell Death Differ.* **29**, 1364–1378 (2022).
38. Jouan, Y. et al. Lin28a induces SOX9 and chondrocyte reprogramming via HMGA2 and blunts cartilage loss in mice. *Sci. Adv.* **8**, eabn3106 (2022).
39. Zhang, S. et al. Hnrnpk protects against osteoarthritis through targeting WWC1 mRNA and inhibiting Hippo signaling pathway. *Mol. Ther.* **32**, 1461–1478 (2024).
40. McDermott, B. T., Ellis, S., Bou-Gharios, G., Clegg, P. D. & Tew, S. R. RNA binding proteins regulate anabolic and catabolic gene expression in chondrocytes. *Osteoarthr. Cartil.* **24**, 1263–1273 (2016).
41. Zhang, H. et al. Mechanical overloading promotes chondrocyte senescence and osteoarthritis development through downregulating FBXW7. *Ann. Rheum. Dis.* **81**, 676–686 (2022).

42. Hattori, A. et al. Cancer progression by reprogrammed BCAA metabolism in myeloid leukaemia. *Nature* **545**, 500–504 (2017).
43. Suo, J. et al. The RNA-binding protein Musashi2 governs osteoblast-adipocyte lineage commitment by suppressing PPARγ signaling. *Bone Res* **10**, 31 (2022).
44. Smith, T. J. et al. Engineered IgM and IgG cleaving enzymes for mitigating antibody neutralization and complement activation in AAV gene transfer. *Mol. Ther.* **32**, 2080–2093 (2024).
45. He, A. T., Liu, J., Li, F. & Yang, B. B. Targeting circular RNAs as a therapeutic approach: current strategies and challenges. *Signal Transduct. Target Ther.* **6**, 185 (2021).
46. Liu, C. X. & Chen, L. L. Circular RNAs: Characterization, cellular roles, and applications. *Cell* **185**, 2390 (2022).
47. Mailliot, J. & Martin, F. Viral internal ribosomal entry sites: four classes for one goal. *Wiley Interdiscip Rev. RNA* **9** (2018).
48. Kwan, T. & Thompson, S. R. Noncanonical translation initiation in eukaryotes. *Cold Spring Harb. Perspect. Biol.* **11** (2019).
49. Hassett, K. J. et al. Optimization of lipid nanoparticles for intramuscular administration of mRNA vaccines. *Mol. Ther. Nucleic Acids* **15**, 1–11 (2019).
50. Ramishetti, S. et al. A combinatorial library of lipid nanoparticles for RNA delivery to leukocytes. *Adv. Mater.* **32**, e1906128 (2020).
51. Kon, E., Elia, U. & Peer, D. Principles for designing an optimal mRNA lipid nanoparticle vaccine. *Curr. Opin. Biotechnol.* **73**, 329–336 (2022).
52. Chen, C. K. et al. Structured elements drive extensive circular RNA translation. *Mol. Cell* **81**, 4300–4318 e4313 (2021).
53. Huang, Y. & Wang, Z. Therapeutic potential of SOX family transcription factors in osteoarthritis. *Ann. Med.* **57**, 2457520 (2025).
54. Sun, Z. et al. Single-cell RNA sequencing reveals different chondrocyte states in femoral cartilage between osteoarthritis and healthy individuals. *Front Immunol.* **15**, 1407679 (2024).
55. Jing, Y. et al. Genome-wide CRISPR activation screening in senescent cells reveals SOX5 as a driver and therapeutic target of rejuvenation. *Cell Stem Cell* **30**, 1452–1471.e1410 (2023).
56. Yang, W. et al. Msi2-mediated MiR7a-1 processing repression promotes myogenesis. *J. Cachexia Sarcopenia Muscle* **13**, 728–742 (2022).
57. Yi, Q. et al. RNA binding proteins in osteoarthritis. *Front Cell Dev. Biol.* **10**, 954376 (2022).
58. Das Neves Borges, P., Vincent, T. L. & Marenzana, M. Automated assessment of bone changes in cross-sectional micro-CT studies of murine experimental osteoarthritis. *PLoS ONE* **12**, e0174294 (2017).
59. Bitounis, D., Jacquinet, E., Rogers, M. A. & Amiji, M. M. Strategies to reduce the risks of mRNA drug and vaccine toxicity. *Nat. Rev. Drug Discov.* **23**, 281–300 (2024).
60. De La Vega, R. E. et al. Efficient healing of large osseous segmental defects using optimized chemically modified messenger RNA encoding BMP-2. *Sci. Adv.* **8**, eabl6242 (2022).
61. Hou, X., Zaks, T., Langer, R. & Dong, Y. Lipid nanoparticles for mRNA delivery. *Nat. Rev. Mater.* **6**, 1078–1094 (2021).
62. Chatterjee, S., Kon, E., Sharma, P. & Peer, D. Endosomal escape: A bottleneck for LNP-mediated therapeutics. *Proc. Natl. Acad. Sci. USA* **121**, e2307800120 (2024).
63. Jeong, M., Lee, Y., Park, J., Jung, H. & Lee, H. Lipid nanoparticles (LNPs) for in vivo RNA delivery and their breakthrough technology for future applications. *Adv. Drug Deliv. Rev.* **200**, 114990 (2023).
64. Suo, J. et al. Accelerated aging in articular cartilage by ZMPSTE24 deficiency leads to osteoarthritis with impaired metabolic signaling and epigenetic regulation. *Cell Death Dis.* **14**, 336 (2023).
65. Glasson, S. S., Chambers, M. G., Van Den Berg, W. B. & Little, C. B. The OARSI histopathology initiative - recommendations for histological assessments of osteoarthritis in the mouse. *Osteoarthr. Cartil.* **18**, S17–S23 (2010).
66. Cheng, Q. et al. Selective organ targeting (SORT) nanoparticles for tissue-specific mRNA delivery and CRISPR-Cas gene editing. *Nat. Nanotechnol.* **15**, 313–320 (2020).
67. Ji, Q. et al. Single-cell RNA-seq analysis reveals the progression of human osteoarthritis. *Ann. Rheum. Dis.* **78**, 100–110 (2019).

Acknowledgements

This work was supported by the Strategic Priority Research Program of the Chinese Academy of Science (grant no: XDB0570000 to W.Z. and L.C.), Science and Technology Commission of Shanghai Municipality (STCSM) (grant nos. 23DX1900101 and 23DX1900100 to W.Z. and L.C.; 24ZR1473500 to Y.H.), the National Natural Science Foundation of China (NSFC) (grant nos. 82202742, 82572822 to J.S.; 82230082 and 81991512 to W.Z.), CAS Project for Young Scientists in Basic Research, Grant No. YSBR-077, the National Key Research and Development Program of China (grant no: 2022YFA0806600 to W.Z., 2021YFA1300501 to L.C.), the Space Medical Experiment Project of China Manned Space Program, Grant No. HYZHXM01025. This study was supported by the National Youth Talent Project of Shanghai Sixth People's Hospital (ynqnpy202501 to J.S.). We thank the Chen laboratory members and Zou laboratory members for critical discussion. We thank the animal platform and cell platform of the Innovation Center of Excellence in Molecular and Cellular Sciences of the Chinese Academy of Sciences for providing convenient services for the experiments involved in this project. We also thank the National Center for Orthopaedic Medicine/Shanghai Institute of Micrographic Surgery of the Extremities platform for their assistance.

Author contributions

W.Z., L.C., J.S., and Y.H. designed, conceived, and supervised the study. G.L. and W.T. were responsible for the analysis of AAV injections and phenotypes and provided clinical samples of human joint sections. J.S. conceived and designed the study, performed the animal experiments, analyzed the data, and wrote the manuscript. L.L., Y.H., S.G., B.G., Y.W., M.W., and X.G. made the constructs, performed ivcRNA-LNPs encapsulation, J.S., L.L., and Y. H. analyzed the data, article modification, and revised the manuscript. P.H. provided *Msi2* knockout mice. J.S. and J.W. provided genetic strains of mice, establish DMM model. X.Y. and S.S. were responsible for immuno-histochemical staining and performed quantitative statistical analyses. J. F. cultured the cells and WB. R.S., L.W., H.F., and X.Z. provided valuable suggestions.

Competing interests

W.Z., L.C., J.S., and L.L. are named as inventors on patents related to circRNA held by CAS CEMCS. L.C. is a scientific co-founder of RiboX Therapeutics. The remaining authors declare no competing interests.

Additional information

Supplementary information The online version contains supplementary material available at https://doi.org/10.1038/s41467-025-63343-z.

Correspondence and requests for materials should be addressed to Jinlong Suo, Guanghua Lei, Youkui Huang or Weiguo Zou.

Peer review information *Nature Communications* thanks Susanne Grässel, Albrecht Bindereif and the other, anonymous, reviewer(s) for their contribution to the peer review of this work. A peer review file is available.